Bachelorarbeit
Zur Erlangung des akademischen Grades Bachelor of Science

Berechnung der elastischen Konstanten zweiter Ordnung von Perovskiten

eingereicht von: Henry Herrmann

Gutachter/innen: PD Pasquale Pavone
Prof. Claudia Draxl

Eingereicht am Institut für Physik der Humboldt-Universität zu Berlin
am: 06.04.2026

Calculation of the Second-Order Elastic Constants of Perovskites

Henry Herrmann

Thesis presented for the degree of
"Bachelor of Science"

Humboldt-Universität zu Berlin
Faculty of Mathematics and Natural Sciences
Department of Physics

Examiners:

1) PD Pasquale Pavone 2) Prof. Claudia Draxl

Thesis submitted on April 6, 2026

Abstract

Finding out the elastic properties of materials is essential for their use in many technological applications. In this thesis, we compute the second-order elastic constants of perovskite materials. For this, we make use of Kohn-Sham density-functional theory (DFT) within the **exciting** code [1] which applies a linearized augmented plane wave + local orbital (LAPW+lo) basis. Our calculations are carried out using the **ElaStic** tool [2]. We employ a selection of exchange-correlation functionals, starting from the local-density approximation (LDA) and going up Jacob's ladder [3] of complexity to hybrid functionals like the Heyd–Scuseria–Ernzerhof functional (HSE). This thesis presents a purely theoretical approach, without relying on empirical data. The results are compared with the available experimental values. Our workflow starts with an initial structural relaxation, followed by a convergence study of the necessary input parameters, including **rgkmax**, **ngridk**, and **gmaxvr**, to achieve a numerical precision below 1 Gigapascal and down to 0.1 Gigapascal in some cases.

Contents

Introduction **1**

1 Theoretical background **3**

1.1 Theory of elasticity 3

1.2 Computation of elastic constants 8

1.3 The total energy of a crystal 9

1.4 Density-functional theory 10

1.5 Exchange-correlation functionals 13

1.5.1 The local-density approximation 14

1.5.2 Generalized-gradient approximations 14

1.5.3 Hybrid functionals 15

1.6 Numerical solution of the KS equations 16

2 Materials **17**

3 Method **23**

3.1 The **exciting** package 23

3.2 The **ElaStic** workflow 27

4 Results **33**

4.1 Barium stannate ($BaSnO_3$) 34

4.2 Caesium lead iodide ($CsPbI_3$) 37

4.3 Lanthanum indium oxide ($LaInO_3$) 41

4.4 Discussion 43

Conclusions and Outlook **47**

Bibliography **49**

A Species files **61**

B Input files **65**

C Convergence studies **67**

D Diamond reference calculations **71**

Introduction

Crystals show a specific elastic response when stress is applied to them, for instance, a change in volume or shape of the unit cell. The elastic properties of a material describe this elastic response. This quantitative knowledge can be applied to the manufacturing of semiconductors [4] and biomedical materials [5]. Elastic constants of a material give us insight into its stability, stiffness, and anisotropy. In particular, the second-order elastic constants (SOECs) are of high importance, as they define the linear elastic response and allow the derivation of material parameters such as the bulk modulus and shear modulus, which are essential for predicting the behavior of the crystal under relatively low pressure.

Perovskite materials are very versatile crystal systems due to their highly tunable structural, electronic, and mechanical properties [6]. They show high flexibility, enabling the integration of cations and anions to tune conductivity for applications in photovoltaics and superconductor technology [7]. Their formula is ABX_3, where X is taken by oxygen for most structures [8].

First-principles (*ab initio*, meaning not derived from experiments) calculations based on density-functional theory (DFT) have become essential in the theoretical research around material properties, achieving good predictions that avoid empirical parameters as input entirely. The **`exciting`** code [1] is a full-potential all-electron implementation of the linearized augmented plane wave + local orbital (LAPW+lo) method. By using it to find the energies of crystal structures for different strains, this thesis aims to calculate the second-order elastic constants and the elastic tensor of selected perovskite materials: Barium stannate ($BaSnO_3$) and caesium lead iodide ($CsPbI_3$) in the cubic crystal structures and lanthanum indium oxide ($LaInO_3$) in the orthorhombic crystal structure.

The computational workflow of this study begins with structural relaxations to obtain equilibrium geometries with no residual forces. For this, the Birch-Murnaghan equation of state (BM-EOS) is used, an established model for describing the equation of state of solids [9]. Then, a convergence analysis of fundamental computational parameters, including **`rgkmax`**, **`ngridk`**, and **`gmaxvr`**, is made to achieve accurate values for the elastic constants and sufficient numerical precision. The elas-

tic tensor is derived through applying small deformations to the optimized structure, then performing **exciting** calculations, and analyzing the resulting energy-strain relations with polynomial fits. For this, we use the **ElaStic** tool [2] for **exciting**. The computed data will be uploaded to the NOMAD repository [10] to serve as benchmark data for future studies.

The structure of this thesis is as follows: Chapter 1 presents a theoretical overview of elasticity and Kohn-Sham DFT. Chapter 2 introduces the perovskite materials investigated in this study. Chapter 3 deals with the computational methodology and the several convergence criteria. Chapter 4 presents the results and gives a comparative analysis. Finally, we summarize the findings and give an outlook.

Chapter 1

Theoretical background

Here, we give a compact overview of the theoretical background that is necessary to understand the calculations performed in this thesis. First, we look at the theory of elasticity in solids and introduce the elastic constants and how to compute them. Then, we briefly discuss the theory that allows the explicit calculation of the total elastic energy of a crystal, density-functional theory (DFT). In particular, we mention the exchange-correlation functionals that are used in this work.

1.1 Theory of elasticity

In order to investigate the deformation of a crystal, we introduce the mathematical framework to describe it accurately. What interests us is the relation between the stress σ—a generalization of the concept of pressure that is applied on a solid—and the strain ϵ, which describes the resulting change in volume or shape of the solid the stress was applied to. Simplified, stress is equal to the external forces on the solid per unit area [11]: $\sigma = F/A$. This work focuses on linear elasticity, which assumes that the strain ϵ and stress σ are directly proportional by a constant, the elastic constant C,

$$\sigma = C \cdot \epsilon \quad . \tag{1.1}$$

This is valid for small deformations, where the solid returns to the equilibrium structure once the stress is relieved [12]. It is Hooke's Law of elasticity. The goal of this section is to arrive at a more generalized expression for this relation in 3 dimensions—accounting for the symmetry of the crystal—that we can later use to compute its elastic constants.

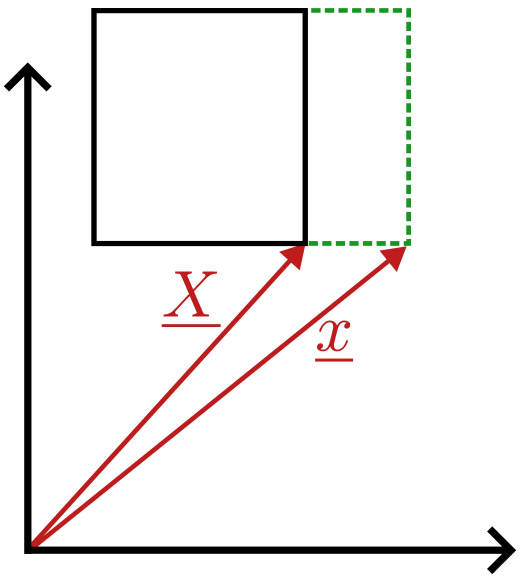

Figure 1.1: The unit cell of a 2 dimensional solid is stretched horizontally. The vectors $\underline{X}$ and $\underline{x}$ point to the position of a single atom in the lattice before and after the deformation.

In order to map out the strain, we look at a 2 dimensional solid as an example, see Figure 1.1. If $\underline{X}$ is the vector denoting the position of an atom of the crystal structure in space, then this point will shift to a new position $\underline{x}$ after a deformation has taken place. This transformation can be described with the deformation matrix $\underline{\underline{J}}$, which consists of the identity matrix $\underline{\underline{\mathbb{1}}}$ and the so-called physical strain matrix $\underline{\underline{\epsilon}}$:

$$\underline{x} = \underline{\underline{J}} \cdot \underline{X} = (\underline{\underline{\mathbb{1}}} + \underline{\underline{\epsilon}}) \cdot \underline{X} \,. \tag{1.2}$$

The physical strain $\underline{\underline{\epsilon}}$ takes the form of a symmetric 3×3 matrix. In 2 dimensions it would be a 2×2 matrix:

$$\underline{\underline{\epsilon}} = \begin{pmatrix} \epsilon_{xx} & \epsilon_{xy} & \epsilon_{xz} \\ \epsilon_{xy} & \epsilon_{yy} & \epsilon_{yz} \\ \epsilon_{xz} & \epsilon_{yz} & \epsilon_{zz} \end{pmatrix}; \qquad \underline{\underline{\epsilon}} \overset{\text{2D}}{=} \begin{pmatrix} \epsilon_{xx} & \epsilon_{xy} \\ \epsilon_{xy} & \epsilon_{yy} \end{pmatrix}. \tag{1.3}$$

The deformation that can be seen in Figure 1.1 is a uniaxial deformation (along one axis only). This can be achieved with the following $\underline{\underline{\epsilon}}$ matrix:

$$\underline{\underline{\epsilon}} = \begin{pmatrix} \epsilon_{xx} & 0 \\ 0 & 0 \end{pmatrix}. \tag{1.4}$$

Other types of strain include expansions/compressions or shear strains which can be seen in Figure 1.2 in 2 dimensions.

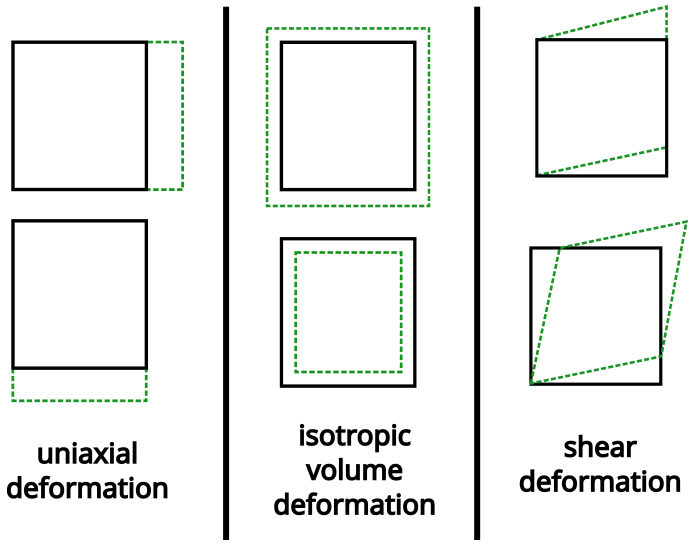

Figure 1.2: Different kinds of deformations/strains that can be applied to a material.

The physical strain is not thermodynamically invariant under translations and rotations. To ensure thermodynamic invariance, we need to define a new type of strain by looking at the difference in the norm of a line element in the solid before ($|\underline{\mathrm{d}X}|$) and after ($|\underline{\mathrm{d}x}|$) the deformation [13]:

$$|\underline{\mathrm{d}x}|^2 - |\underline{\mathrm{d}X}|^2 \overset{\text{def}}{=} 2\, \underline{\mathrm{d}X} \cdot \underline{\underline{\eta}} \cdot \underline{\mathrm{d}X}\,. \tag{1.5}$$

This new kind of strain, $\underline{\underline{\eta}}$ in Eq. (1.5), is the so-called Lagrangian strain. Now, drawing from Eq. (1.2) we can use:

$$\underline{\mathrm{d}x} = \underline{\underline{J}} \cdot \underline{\mathrm{d}X}\,, \tag{1.6}$$

and obtain the following:

$$\underline{\mathrm{d}X} \cdot \underline{\underline{J}}^T \underline{\underline{J}} \cdot \underline{\mathrm{d}X} - \underline{\mathrm{d}X} \cdot \underline{\mathrm{d}X} = 2\, \underline{\mathrm{d}X} \cdot \underline{\underline{\eta}} \cdot \underline{\mathrm{d}X}\,. \tag{1.7}$$

Here we can identify $\underline{\underline{\eta}} = \left(\underline{\underline{J}}^T \underline{\underline{J}} - \underline{\underline{\mathbb{1}}}\right)/2$ and with $\underline{\underline{J}} = \underline{\underline{J}}^T = \underline{\underline{\mathbb{1}}} + \underline{\underline{\epsilon}}$ we find the following expression for the Lagrangian strain in terms of $\underline{\underline{\epsilon}}$:

$$\underline{\underline{\eta}} = \underline{\underline{\epsilon}} + \frac{1}{2}\,\underline{\underline{\epsilon}}^2\,. \tag{1.8}$$

If the strain $\underline{\underline{\epsilon}}$ is sufficiently small, then $\underline{\underline{\eta}} \approx \underline{\underline{\epsilon}}$. Also, it follows directly from Eq. (1.8)

that $\underline{\underline{\eta}}$ too is a symmetric 3×3 matrix:

$$\underline{\underline{\eta}} = \begin{pmatrix} \eta_{xx} & \eta_{xy} & \eta_{xz} \\ \eta_{xy} & \eta_{yy} & \eta_{yz} \\ \eta_{xz} & \eta_{yz} & \eta_{zz} \end{pmatrix} . \tag{1.9}$$

To reduce complexity it is advisable to employ the Voigt notation [11] which uses only the six independent components and arranges them into a vector:

$$\underline{\eta} \overset{\text{def}}{=} (\eta_{xx}, \eta_{yy}, \eta_{zz}, 2\eta_{yz}, 2\eta_{xz}, 2\eta_{xy}) = (\eta_1, \eta_2, \eta_3, \eta_4, \eta_5, \eta_6) . \tag{1.10}$$

The entries of the off-diagonal part of the matrix appear twice in the vector because they also appear twice in the matrix, making notation easier for summations. For the rest of this thesis, we use the Voigt notation.

The external forces acting upon the material must be cancelled out exactly by internal forces in the opposite direction, otherwise the crystal would not reach a new equilibrium position. These internal forces must come with a change in the potential energy per equilibrium crystal volume $\Delta\tilde{E} = \Delta E/V_0$. To express this elastic energy density $\tilde{E} = E/V_0$ as a function of strain, we expand the energy into a Taylor series in terms of the Lagrangian strain (using the Voigt notation). The reference position for the expansion is the equilibrium—here all forces are absent, the stress is zero. The expansion reads as follows:

$$\begin{aligned} \tilde{E}(\underline{\eta}) = \tilde{E}(\underline{\eta} = 0) & \\ + \sum_{i=1}^{6} \left.\frac{\partial \tilde{E}}{\partial \eta_i}\right|_{\underline{\eta}=0} \eta_i & \\ + \frac{1}{2} \sum_{i=1}^{6}\sum_{j=1}^{6} \left.\frac{\partial^2 \tilde{E}}{\partial \eta_i \partial \eta_j}\right|_{\underline{\eta}=0} \eta_i\, \eta_j & \\ + \frac{1}{6} \sum_{i=1}^{6}\sum_{j=1}^{6}\sum_{k=1}^{6} \left.\frac{\partial^3 \tilde{E}}{\partial \eta_i \partial \eta_j \partial \eta_k}\right|_{\underline{\eta}=0} \eta_i\, \eta_j\, \eta_k \;+\; \mathcal{O}(\eta^4) . & \end{aligned} \tag{1.11}$$

Here, $\tilde{E}(\underline{\eta} = 0)$ is the energy in equilibrium. The term $\partial\tilde{E}/\partial\eta_i\,|_{\underline{\eta}=0}$ is the change of energy at zero strain—at the minimum of the energy-strain curve—and has to vanish because of the equilibrium condition for the reference system. The constants appearing in the second-order term of the expansion are the second-order elastic constants (SOECs):

$$C_{ij} = \left.\frac{\partial^2 \tilde{E}(\underline{\eta})}{\partial \eta_i \partial \eta_j}\right|_{\underline{\eta}=0} . \tag{1.12}$$

The SOECs describe how much the energy changes when applying a strain in a small region around the reference equilibrium configuration. They are related to the curvature of the energy-strain curve at zero strain, hence, they describe how much energy has to be put into the system to achieve a certain deformation, meaning that they are indicators of the stiffness of a solid. The elastic constants of higher order can be found in the higher-order terms in the expansion. This thesis studies only the SOECs, thus we ignore the other terms in Eq. (1.11) and arrive at the following change in elastic energy due to deformation, using the Einstein notation:

$$\Delta\tilde{E}(\underline{\eta}) = \frac{1}{2}\, C_{ij}\, \eta_i\, \eta_j \ . \tag{1.13}$$

Looking at the derivative of this expression:

$$\frac{\partial\tilde{E}(\underline{\eta})}{\partial\eta_i} = C_{ij}\, \eta_j \ , \tag{1.14}$$

we find the same structure as in Eq. (1.1). Thus, Eq. (1.14) can be considered the 3 dimensional analogue of Eq. (1.1) using Lagrangian instead of physical strain. However, we note that when using physical strain the values for the SOECs are actually identical. One can verify this by putting the definition of Lagrangian strain in Eq. (1.8) into the expansion in Eq. (1.11). Since the linear term vanishes the prefactor in the order of ϵ^2 will still be C_{ij}. This only applies for the second-order elastic constants and not for higher-order terms [14].

The constants C_{ij} are the components of the elastic tensor $\underline{\underline{C}}$. In Voigt notation this is a 6×6 matrix:

$$\underline{\underline{C}} = \begin{pmatrix} C_{11} & C_{12} & C_{13} & C_{14} & C_{15} & C_{16} \\ C_{21} & C_{22} & C_{23} & C_{24} & C_{25} & C_{26} \\ C_{31} & C_{32} & C_{33} & C_{34} & C_{35} & C_{36} \\ C_{41} & C_{42} & C_{43} & C_{44} & C_{45} & C_{46} \\ C_{51} & C_{52} & C_{53} & C_{54} & C_{55} & C_{56} \\ C_{61} & C_{62} & C_{63} & C_{64} & C_{65} & C_{66} \end{pmatrix} . \tag{1.15}$$

The diagonal components C_{11}, C_{22}, and C_{33} refer to the uniaxial deformations in the x-, y-, and z-direction, respectively. The components C_{44}, C_{55}, and C_{66} refer to the stiffness of the material for pure shear distortions. The off-diagonal components refer to the coupling of different directions: How great the tendency of the material is to expand or contract in a direction perpendicular to the direction the original strain was applied in. Just as well the material could show a shear stress in directions different from the direction of the strain. The tensor being symmetric is then

equivalent to saying that the applied deformation and the resulting stress in other directions are exchangeable. High values of the elastic constants are a sign of stiff materials, while lower values are a sign of soft materials. This becomes obvious by looking at the Hooke's law of elasticity in Eq. (1.1): The higher C, the higher the necessary stress σ to achieve the same strain ϵ.

For an actual crystal, the present crystal symmetry allows us to further simplify this matrix. For instance, in a crystal with cubic symmetry the tensor $\underline{\underline{C}}$ only consists of three independent non-zero components C_{11}, C_{12}, and C_{44} [15]. The elastic tensor in this case is:

$$\underline{\underline{C}} = \begin{pmatrix} C_{11} & C_{12} & C_{12} & & & & \\ C_{12} & C_{11} & C_{12} & & & & \\ C_{12} & C_{12} & C_{11} & & & & \\ & & & C_{44} & & & \\ & & & & C_{44} & & \\ & & & & & C_{44} & \end{pmatrix}, \tag{1.16}$$

where an empty entry means that the corresponding C_{ij} vanishes. Any zero component indicates that the respective deformations are entirely decoupled, one does not influence the other.

1.2 Computation of elastic constants

In order to calculate the elastic constants, we first need to obtain the energy of the crystal as a function of deformation. The next sections will deal with this problem. Now, assuming that we already have this information (meaning the curvature of the energy-strain curve at zero strain during a given type of deformation), we still have to determine to which combination of the C_{ij} these curvature values correspond. In general, the curvature is a certain linear combination of the SOECs in Eq. (1.15), depending on the crystal structure and the distortion.

For simplicity, we take a cubic crystal structure as an example, reducing the number of SOECs to three. Inserting the values from Eq. (1.16) into Eq. (1.13), the change in the energy density after distortion, yields:

$$\Delta\tilde{E} = \frac{1}{2}\,C_{11}\left(\eta_1^2+\eta_2^2+\eta_3^2\right) + C_{12}\left(\eta_1\,\eta_2+\eta_1\,\eta_3+\eta_2\,\eta_3\right) + \frac{1}{2}C_{44}\left(\eta_4^2+\eta_5^2+\eta_6^2\right). \tag{1.17}$$

Let us assume the distortion is the isotropic volume deformation shown in Figure 1.2.

The Lagrangian strain corresponding to this deformation is:

$$\underline{\eta} = (\eta, \eta, \eta, 0, 0, 0)\,, \tag{1.18}$$

where η is a parameter determining the size of the strain. Plugging this into Eq. (1.17), we get:

$$\Delta\tilde{E} = \frac{3}{2}\,(C_{11} + 2C_{12})\,\eta^2\,. \tag{1.19}$$

This allows us to identify the linear combination of SOECs that describes the energy curvature for an isotropic expansion around the reference equilibrium configuration. In this expression one can identify the so-called bulk modulus for cubic systems $B = (C_{11} + 2C_{12})/3$, describing the necessary change in external isotropic pressure to lead to a certain change in volume of the sample.

If we now repeat the steps of Eqs. (1.18) to (1.19) for two other distortions, then we have a linear system of three equations which will be enough to calculate the three independent elastic constants C_{11}, C_{12}, and C_{44}. The number of distortions we have to compute the energies for is always the same as the amount of independent constants in the elastic tensor $\underline{\underline{C}}$ for the system.

1.3 The total energy of a crystal

As seen in the previous paragraphs, the main ingredient for the computation of the elastic constants is the total energy of a crystal—a stationary system of N_n nuclei and N_e electrons—as a function of deformation. In principle, what we would have to do is to solve the time-independent Schrödinger equation (without external fields):

$$\hat{H}\,\Psi(r, R) = \mathcal{E}\,\Psi(r, R)\ , \tag{1.20}$$

where $\hat{H}$ is the Hamiltonian of the system and $\Psi(r, R)$ is the eigenstate with the corresponding eigenvalue $\mathcal{E}$. $\Psi(r, R)$ represents the wave function of the system of all nuclei and electrons and thus depends on two sets of variables: The coordinates of the electrons $r = \{\underline{r}_1, ..., \underline{r}_{N_\mathrm{e}}\}$ and the nuclear coordinates $R = \{\underline{R}_1, ..., \underline{R}_{N_\mathrm{n}}\}$. The Hamiltonian $\hat{H}$ consists of the kinetic energies and the potential energies that result from Coulomb forces between the nuclei and electrons:

$$\hat{H}(r, R) = \hat{T}_\mathrm{n}(R) + \hat{T}_\mathrm{e}(r) + \hat{V}_\mathrm{nn}(R) + \hat{V}_\mathrm{ee}(r) + \hat{V}_\mathrm{en}(r, R)\,, \tag{1.21}$$

where $\hat{T}$ is the kinetic energy operator and $\hat{V}$ is the electrostatic Coulomb potential with the subscripts specifying between which charged particles, (n) for nuclei and (e) for electrons. For our purposes, we do not need to solve the full problem

with $3N_\mathrm{n} + 3N_\mathrm{e}$ degrees of freedom, which anyway would be an impossible task for complex systems.

To simplify the problem, we employ the Born-Oppenheimer approximation [16], which assumes that, due to their highly different masses, nuclei and electrons are moving on highly different time scales, making it possible to treat their wave functions separately. Using the Born-Oppenheimer approximation, and assuming that the nuclei are clamped at their positions R, we can evaluate the total energy of our system of electrons and clamped ions by solving the Schrödinger equation for the electronic Hamiltonian $\hat{H}_\mathrm{e}$ only (note the changes in notation):

$$\begin{aligned} \hat{H}_\mathrm{e}(r) &= \hat{T}_\mathrm{e}(r) + \hat{V}_\mathrm{en}(r) + V_\mathrm{nn} + \hat{V}_\mathrm{ee}(r) \\ &\stackrel{\mathrm{def}}{=} \hat{T} \quad + \quad \hat{V} \quad + \quad \hat{W} \quad , \end{aligned} \tag{1.22}$$

where the dependence on R is parametric only and V_nn is just a constant offset. The Schrödinger equation reads:

$$\hat{H}_\mathrm{e}\,\varphi(r) = E_\mathrm{tot}\,\varphi(r)\ , \tag{1.23}$$

where E_tot is the ground-state (GS) energy of the electronic system and $\varphi(r)$ is the electronic wave function. From now on, we focus on the GS solution of Eq. (1.23).

1.4 Density-functional theory

In an effort to further reduce complexity in the determination of the solution of Eq. (1.23), the idea of density-functional theory (DFT)[1] is to use the electron density $n(\underline{r})$ as a main quantity instead of a wave function dependent on the coordinates of every electron. This drastically reduces the degrees of freedom from $3\,N_\mathrm{e}$ to just 3. That choice is justified by the Hohenberg-Kohn theorem [17], which states that the GS energy of a system of interacting electrons, E_GS, can be written as a functional of the electron density:

$$E_\mathrm{GS} = E[n_\mathrm{GS}]\,. \tag{1.24}$$

The goal now would be to find the exact form of this energy functional. We can write in the Dirac notation:[2]

$$E[n] = \langle\varphi[n]\,|\,\hat{H}_\mathrm{e}\,|\,\varphi[n]\rangle = T[n] + V[n] + W[n]\,. \tag{1.25}$$

[1] For our description, we roughly follow Ref. [11], where a more detailed explanation of density-functional theory can be found.

[2] The existence of this expression is not trivial, since n here is a general density as opposed to the GS density n_GS. The question whether the energy can be written as a functional of a general density is a question that research around v-representability [18] is concerned with. However, in most cases we can assume that $E[n]$ exists for a density that is normalized to the number of electrons N_e.

The problem is that we do not know how to express $T[n]$ and $W[n]$ in terms of the density. In other words, the forms of the functionals $T[n]$ and $W[n]$ are unknown. The solution proposed by Kohn and Sham [19] is to split this expression into parts that are in fact known and a part that accounts for the difference ($E_{\mathrm{xc}}[n]$). For the known part a fictional system of independent non-interacting electrons is assumed.

$$E[n] = T_0[n] + V[n] + E_{\mathrm{H}}[n] + E_{\mathrm{xc}}[n]\,. \tag{1.26}$$

Here, $V[n]$ is the external potential energy:

$$V[n] = \langle \varphi[n] \,|\, \hat{V} \,|\, \varphi[n] \rangle = \int \mathrm{d}^3 r \; n(\underline{r})\, v(\underline{r})\,, \tag{1.27}$$

which is the integral over all the contributions of the Coulomb energies of the nuclei in the material, $v(\underline{r}) = \sum_{\nu=1}^{N_{\mathrm{n}}} (Z_\nu / |\underline{r} - \underline{R}_\nu|) + V_{\mathrm{nn}}$ (where Z_ν is the respective nuclear charge). It can be expressed with an explicit dependence on $n(\underline{r})$ as a continuous analogue of electrons feeling the nuclear potential at positions $\underline{r}$.

$E_{\mathrm{H}}[n]$ is the so-called Hartree energy:

$$E_{\mathrm{H}}[n] = \frac{1}{2} \iint \mathrm{d}^3 r \, \mathrm{d}^3 r' \; \frac{n(\underline{r})\, n(\underline{r}')}{|\underline{r} - \underline{r}'|}\;. \tag{1.28}$$

This term describes the electrostatic energy of an electron density $n(\underline{r})$. It is a part of the interaction energy of electrons $W[n]$, but it is not quantum-mechanical in nature and therefore misses the exchange effects and the correlation of electrons with each other as particles.

$T_0[n]$ is the kinetic energy of a system of single non-interacting electrons:

$$T_0[n] = -\sum_i^{\mathrm{occ.}} \int \mathrm{d}^3 r \; \tilde{\varphi}_i^*(\underline{r})\, \frac{\nabla^2}{2}\, \tilde{\varphi}_i(\underline{r})\,, \tag{1.29}$$

where $\tilde{\varphi}_i(\underline{r})$ is an independent electron state. Note that the dependence on the density here is still just implicit. One can only compute this value by knowing the wave functions $\tilde{\varphi}_i(\underline{r})$. It is important to remember that these electrons carry no physical meaning, the interaction operator $\hat{W}$ is zero for them. Yet they reproduce the same energy as the system of interacting particles, simply because this is the condition on which the extra term in Eq. (1.26), $E_{\mathrm{xc}}[n]$, was defined. This term is called the exchange-correlation functional. It includes all that was neglected by this description, namely:

- exchange energy—arising from the antisymmetry of the wave function according to the Pauli exclusion principle [20].

- correlation energy—including the effects of electron-electron coupling arising from the repulsion of particles with the same charge and also dynamical effects depending on the movement of electrons.[3]

The contents of $E_{\mathrm{xc}}[n]$ are unknown though and have to be approximated. In Section 1.5 the approximations used in this thesis are presented.

Now, by the variational principle [11], if there exists a GS density n_{GS} then it has to be the one that minimizes the energy functional:

$$E[n] > E[n_{\mathrm{GS}}] = E_{\mathrm{GS}},\ \forall n \neq n_{\mathrm{GS}}\,. \tag{1.30}$$

In order to find n_{GS} we apply a constrained minimization of $E[n]$, demanding that the wave functions $\tilde{\varphi}_i(\underline{r})$ satisfy the orthonormality condition,

$$\frac{\delta}{\delta n}\left\{E[n] - \sum_{i,j}\lambda_{ij}\big(\langle\tilde{\varphi}_i|\tilde{\varphi}_j\rangle - \delta_{ij}\big)\right\} = 0\,, \tag{1.31}$$

where λ_{ij} are the Lagrange multipliers. Having performed the minimization,[4] one ends up with the Kohn-Sham (KS) equation [19]:

$$\left[-\frac{1}{2}\nabla^2 + v(\underline{r}) + v_{\mathrm{H}}(\underline{r},[n]) + v_{\mathrm{xc}}(\underline{r},[n])\right]\phi_i(\underline{r}) = \varepsilon_i\,\phi_i(\underline{r})\,, \tag{1.32}$$

where the $\phi_i(\underline{r})$ are the non-physical KS states with respective single-particle energy eigenvalues ε_i, $v(\underline{r})$ describes the external potential from Eq. (1.27), v_H is the Hartree potential:

$$v_{\mathrm{H}}(\underline{r},[n]) = \frac{\delta E_{\mathrm{H}}[n]}{\delta n} = \int \mathrm{d}^3r'\,\frac{n(\underline{r}')}{|\underline{r}-\underline{r}'|}\,, \tag{1.33}$$

and v_{xc} is the exchange-correlation potential:

$$v_{\mathrm{xc}}(\underline{r},[n]) = \frac{\delta E_{\mathrm{xc}}[n]}{\delta n}\,. \tag{1.34}$$

By solving Eq. (1.32) for the $\phi_i(\underline{r})$ the GS density can be computed:

$$n_{\mathrm{GS}}(\underline{r}) = 2\sum_{i=1}^{\mathrm{occ.}}|\phi_i(\underline{r})|^2\,. \tag{1.35}$$

This is simply the probabilities of finding an electron at position $\underline{r}$ of the KS wave functions summed, since they are independent of one another. In principle the basis

[3] This also accounts for the difference of the non-interacting kinetic energy $T_0[n]$ and the interacting kinetic energy [21].

[4] The full procedure can be found in Ref. [11].

set of KS states is infinite, but the sum runs just over the occupied states. The 2 in front of the sum accounts for the fact that every state can contain two KS electrons, one with spin-up and one with spin-down. This density is normalized to the number of electrons in the system N_e because of the orthonormality constraint from above:[5]

$$\int \mathrm{d}^3r \; n_\mathrm{GS}(\underline{r}) = 2\sum_{i=1}^{\mathrm{occ.}} \int \mathrm{d}^3r \; |\phi_i(\underline{r})|^2 = 2\sum_{i=1}^{\mathrm{occ.}} 1 = 2\,N_\mathrm{occ.} = N_\mathrm{e}\,. \tag{1.36}$$

With the help of Eq. (1.32) we can now find the energetic ground state. However, the effective potential in this equation, namely the Kohn-Sham (KS) potential $v_\mathrm{KS}(\underline{r},[n]) = v(\underline{r}) + v_\mathrm{H}(\underline{r},[n]) + v_\mathrm{xc}(\underline{r},[n])$, is still a functional of the density n which in turn depends on the $\phi_i(\underline{r})$. This means that the problem must be solved iteratively: By first making an educated guess for n_GS which will be inspired by the external potential $v(\underline{r})$, then using this density to construct a v_KS. Then, Eq. (1.32) is solved using this potential and the resulting KS states correspond to the configuration with the lowest energy in this trial potential. Then via Eq. (1.35) a new density is constructed which will be a better estimate for the true n_GS than the one we started with. This process is repeated until self-consistency is reached, meaning when the changes in density fall below a certain tolerance value. So finding the GS becomes a problem of numerical convergence. When it is reached, the energy we were looking for at the start of this section can be found by calculating Eq. (1.26).

1.5 Exchange-correlation functionals

There are several functionals we can choose to approximate $E_\mathrm{xc}[n]$ in Eq. (1.26) with varying computational cost and precision. They generally use as a starting point the exact expression [14]:

$$E_\mathrm{xc}[n] = \int \mathrm{d}^3r \; e_\mathrm{xc}\big(\underline{r},[n]\big)\,, \tag{1.37}$$

where $e_\mathrm{xc}(\underline{r},[n])$ is the exchange-correlation energy per crystal volume. We can split this up into the energy per particle $\varepsilon_\mathrm{xc}(\underline{r},[n])$ multiplied by the particles per volume [14], in other words the electron density $n(\underline{r})$, and obtain:

$$E_\mathrm{xc}[n] = \int \mathrm{d}^3r \; n(\underline{r})\; \varepsilon_\mathrm{xc}\big(\underline{r},[n]\big)\,. \tag{1.38}$$

[5] The minimization Eq. (1.31) was diagonalized by employing a new rotated basis set ϕ (see Ref. [11]), as opposed to the $\tilde{\varphi}$ we started with. In this diagonalized equation the Lagrange multipliers take the form of energy eigenvalues for the KS states. Because this was a unitary transformation the orthonormality of the wave functions still holds.

Now we are looking for ways to approximate $\varepsilon_{\mathrm{xc}}(\underline{r}, [n])$. This is a non-local term in the sense that its value at a single point $\underline{r}$ depends on all the values of $n(\underline{r}')$ for any $\underline{r}'$ in the crystal volume.

1.5.1 The local-density approximation

The simplest functional is the local-density approximation (LDA) [19]. It assumes the energy per particle of a uniform electron gas (UEG). The exchange part of this functional is analytically known [11]: $\varepsilon_{\mathrm{x}}^{\mathrm{UEG}}[n] = -3/4 \cdot (3/\pi)^{1/3} \cdot n(\underline{r})^{1/3}$, the correlation part $\varepsilon_{\mathrm{c}}^{\mathrm{UEG}}[n]$ is known by numerical methods that calculate the total energy directly for the electron gas and then subtract from this result the analytically known external potential, the kinetic energy, and the Hartree energy of this simple system [22]. Both only depend on the electron density $n(\underline{r})$ at point $\underline{r}$, so we can write Eq. (1.38) as:

$$E_{\mathrm{xc}}^{\mathrm{LDA}}[n] = \int \mathrm{d}^3 r \; n(\underline{r}) \; \varepsilon_{\mathrm{xc}}^{\mathrm{UEG}}\big(n(\underline{r})\big) \, . \tag{1.39}$$

This is strictly local, since it only depends on the electron density at the point $\underline{r}$, so no long-range correlations are included. In principle, this is a very crude approximation. But it turns out that $\varepsilon_{\mathrm{x}}^{\mathrm{UEG}}$ and $\varepsilon_{\mathrm{c}}^{\mathrm{UEG}}$ compensate each other in such a way that structural properties like the lattice constants in equilibrium and the elastic constants can be computed with surprisingly high accuracy [14] in the LDA. The LDA has proven to be a very effective and low-cost exchange-correlation functional.

1.5.2 Generalized-gradient approximations

One step further, we have the generalized-gradient approximations (GGA), a group of functionals that also include the gradient of the density ∇n at point $\underline{r}$ [21]:

$$E_{\mathrm{xc}}^{\mathrm{GGA}}[n] = \int \mathrm{d}^3 r \; n(\underline{r}) \; \varepsilon_{\mathrm{xc}}^{\mathrm{GGA}}\big(n(\underline{r}), \nabla n(\underline{r})\big) \, . \tag{1.40}$$

This is still semi-local, since it only depends on the immediate surroundings of point $\underline{r}$ via the gradient. GGAs use the LDA as a starting point and refine it with enhancement factors that depend on ∇n. A description of the explicit form of a GGA would be beyond the scope of this thesis, see Ref. [3] for further information about this. The GGA functionals we use in this thesis are known as the Perdew-Burke-Ernzerhof (PBE) [23] and, derived from this, the so-called PBEsol [24], which is a version of PBE optimized for solids [25].

1.5.3 Hybrid functionals

The most expensive exchange-correlation functionals we use in this work are the hybrid functionals. They mix the correlation energy obtained with other density functionals with the exact exchange energy from Hartree-Fock theory [26] that is calculated using the KS states $\phi_i(\underline{r})$ with:[6]

$$E_{\mathrm{x}}^{\mathrm{HF}} = -\frac{1}{2}\sum_{i}^{\mathrm{occ.}}\sum_{j}^{\mathrm{occ.}}\iint \mathrm{d}^3r\,\mathrm{d}^3r'\;\frac{\phi_i(\underline{r})\,\phi_j(\underline{r}')\;\phi_j(\underline{r})\,\phi_i(\underline{r}')}{|\underline{r}-\underline{r}'|}\,. \tag{1.41}$$

Thus, hybrids are strictly non-local exchange-correlation functionals. The PBE0-functional [27] uses PBE for its correlation part and is described by the following mixing equation:

$$E_{\mathrm{xc}}^{\mathrm{PBE0}} = \alpha E_{\mathrm{x}}^{\mathrm{HF}} + (1-\alpha)E_{\mathrm{x}}^{\mathrm{PBE}} + E_{\mathrm{c}}^{\mathrm{PBE}}\,, \tag{1.42}$$

where $\alpha = 0.25$ is the mixing parameter. PBE0 has been shown to take a long time with converging Eq. (1.41) due to the slow decline of the $(|\underline{r}-\underline{r}'|)^{-1}$ term for long distances. The Heyd–Scuseria–Ernzerhof (HSE) [28] tries to make this more efficient by only computing $E_{\mathrm{x}}^{\mathrm{HF}}$ for short-range distances of $\underline{r}$ and $\underline{r}'$, leaving long range entirely up to PBE. HSE is defined by the mixing equation:

$$E_{\mathrm{xc}}^{\mathrm{HSE}} = \alpha E_{\mathrm{x}}^{\mathrm{HF,SR}}(\omega) + (1-\alpha)E_{\mathrm{x}}^{\mathrm{PBE,SR}}(\omega) + E_{\mathrm{x}}^{\mathrm{PBE,LR}}(\omega) + E_{\mathrm{c}}^{\mathrm{PBE}}\,, \tag{1.43}$$

where SR and LR stand for the short- and long-range terms, respectively. α determines the portion of exact exchange included in the short-range interaction and ω is the screening parameter which defines where the transition between short and long range is made.[7] The typical choice here is $\alpha = 0.25$ and $\omega = 0.11$ Bohr^{-1}.

[6] The exact exchange potential follows from a constrained minimization of the energy in Eq. (1.25) when choosing a Slater-determinant of single-particle wave functions as the eigenfunctions [11]. The Slater-determinant accounts for the fact that, according to the Fermi principle, the wave function has to behave antisymmetrically under exchange of two electrons.

[7] It does this via the error function $\mathrm{erf}(x)$. In HSE, r^{-1} is redefined through the splitting $1/r = (1-\mathrm{erf}(\omega r))/r + \mathrm{erf}(\omega r)/r$, where the first term vanishes for long distances r and the second term vanishes for short distances r.

1.6 Numerical solution of the KS equations

In practice, the KS states $\phi_i(\underline{r})$ are expanded into a basis set of self-chosen basis functions $\psi_i(\underline{r})$, in Dirac notation:

$$|\phi_i\rangle = \sum_k c_{ik} \, |\psi_k\rangle \, , \tag{1.44}$$

with the coefficients $c_{ik} = \langle\psi_k|\phi_i\rangle$. When plugging Eq. (1.44) into Eq. (1.32) and projecting onto a component j with another bra-vector $\langle\psi_j|$ from the left, we get for the i-th eigenvector:

$$\sum_k c_{ik} \, \langle\psi_j|\hat{H}_{\mathrm{KS}}|\psi_k\rangle = \varepsilon_i \sum_k c_{ik} \, \langle\psi_j|\psi_k\rangle \, , \tag{1.45}$$

where $\hat{H}_{\mathrm{KS}}$ is the full KS Hamiltonian on the left side of Eq. (1.32). We can identify the components of the Hamiltonian in the new basis $H_{jk} = \langle\psi_j|\hat{H}_{\mathrm{KS}}|\psi_k\rangle$ and the components of the overlap matrix $S_{jk} = \langle\psi_j|\psi_k\rangle$. In matrix notation this is a matrix eigenvalue equation [29]:

$$\underline{\underline{H}} \cdot \underline{c}_i = \varepsilon_i \, \underline{\underline{S}} \cdot \underline{c}_i \ , \tag{1.46}$$

where $\underline{c}_i$ is the eigenvector in the new basis. To limit the size of the matrices in Eq. (1.46) , we use a finite basis set and stop the expansion in Eq. (1.44) at a certain k_{max}. The more basis functions you include in the expansion, the more precise your results will be. The choice of the basis depends on the package you are using. This thesis uses the **`exciting`** package and its basis is presented in Section 3.1.

Chapter 2

Materials

This chapter presents the materials that are investigated in this thesis. We look at two materials in the cubic crystal system—barium stannate ($BaSnO_3$) and caesium lead iodide ($CsPbI_3$)—and one in the orthorhombic system—lanthanum indium oxide ($LaInO_3$). They all belong to the perovskite crystal structure which refers to a chemical formula of ABX_3. A and B are always two cations with respective ionic radii R_A and R_B, where generally $R_A > R_B$ [6]. X is taken by an anion with ionic radius R_X. In most cases the anion is oxygen (O), however there are also the so-called halide perovskites for which the X is taken by a halogen, for example iodine (I). The ideal perovskite structure is considered to be the cubic crystal system. In this, the unit cell of a perovskite consists of a BX_6 octahedron with the B-ion in the middle, surrounded by the A-ions on the corners of the cell [8]. This ideal structure can be seen in Figure 2.1.

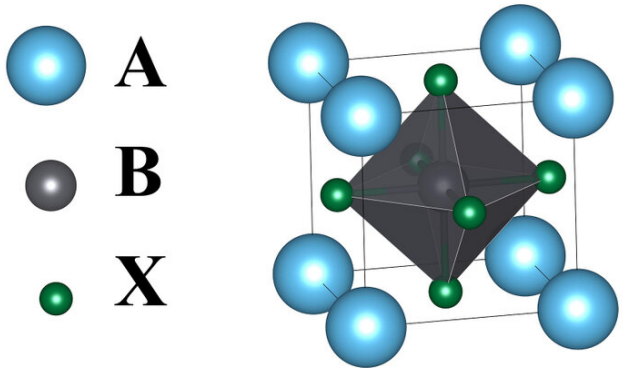

Figure 2.1: The ideal cubic structure of a perovskite crystal. A and B are cations, the X are anions. The image was taken from Ref. [30]

Whether the specific composition of ions will actually crystallize in this structure depends on their ionic radii though. At this point, we could start doing density-functional theory (DFT) calculations to find out if there exists an energetically stable convergent minimum for the cubic structure. However, there is a fairly reliable way to predict it without much computation. Let us assume a unit cell like in Figure 2.1 with the lattice parameter a. In equilibrium, the distance between ions B and X must then be exactly $d_{\mathrm{BX}} = a/2 = R_{\mathrm{B}} + R_{\mathrm{X}}$, since this is how ionic radii are defined.[1] On the other hand, the distance between A and X must be $d_{\mathrm{AX}} = a/\sqrt{2} = R_{\mathrm{A}} + R_{\mathrm{X}}$. Combining these expressions, we get:

$$t = \frac{R_{\mathrm{A}} + R_{\mathrm{X}}}{\sqrt{2}\,(R_{\mathrm{B}} + R_{\mathrm{X}})}\,, \tag{2.1}$$

where in this case $t = 1$, meaning the composition will lie in a perfect cubic structure as per the assumption. t is called the Goldschmidt tolerance factor [31]. In actuality, most perovskites have a t of around 0.75 to 1, but a stable cubic structure can only be achieved for $t \approx 1$. A too small t hints at a size mismatch of the A- and B-ions: If A is too small relative to B, then the octahedra in the middle of the cells will collectively tilt or rotate [32] to reduce the empty space in order to achieve a state of lower energy (with the X-anions and A-cations closer together). In this case the cubic system was not stable and DFT would not have converged to a ground-state energy if cubic input parameters were used for the calculation. The tilt results in a reduction of symmetry, shifting the configuration to a different phase. This is the case for orthorhombic $LaInO_3$. The configuration can also be metastable which actually is the case for $CsPbI_3$, as it can exist in the cubic structure, but also in the orthorhombic structure. This means that a too large deformation of the material can lead to another minimum in the energy-strain curve. This does not affect our calculations for $CsPbI_3$ though, because—dealing with linear elasticity—we look at a sufficiently small region around the energy minimum corresponding to the cubic system.

Even though the perovskite structure was initially defined with a cubic structure in mind [33], crystals with lower symmetry are included in the classification because they all show a 'nearly cubic' [8] structure and often look like cubic crystals on the macroscopic scale too. What makes perovskites especially interesting though, is that a slight tilt of the BX_6 octahedron (a change of phase) can drastically change the electric properties of the solid. For example, an elastic deformation could shift the central octahedron slightly off the center and introduce a polarization caused by an electric dipole moment ("piezoelectricity") [6]. Hence, perovskites attain their highly

[1] Ions are assumed to be effective hard spheres with radius R. The spheres of two ions in equilibrium will be in direct contact to each other.

Table 2.1: The investigated perovskites

Formula	**Crystal system**	**Space group**
$BaSnO_3$	cubic	221-Pm3m
$LaInO_3$	orthorhombic	62-Pnma
$CsPbI_3$	cubic	221-Pm3m

tweakable nature and versatility. Their uses range from insulators to semiconductors up to high-temperature superconductors [7]. The perovskites for which we calculate the second-order elastic constants (SOECs) are listed again in Table 2.1.

$BaSnO_3$ is an oxide perovskite in the cubic structure, especially known for being a wide band gap semiconductor [34]. Its primitive unit cell consists of one barium ion with charge 2+, one tin ion with charge 4+, and three oxygen ions with charge 2−. The Goldschmidt tolerance factor for this composition is $t \approx 0.93$, thus the material is very stable in the cubic system. The lattice is perfectly symmetric, meaning the elastic tensor for this perovskite will look like the one in Eq. (1.16), with only 3 independent SOECs:

$$\underline{\underline{C}} = \begin{pmatrix} C_{11} & C_{12} & C_{12} & & & \\ C_{12} & C_{11} & C_{12} & & & \\ C_{12} & C_{12} & C_{11} & & & \\ & & & C_{44} & & \\ & & & & C_{44} & \\ & & & & & C_{44} \end{pmatrix}. \tag{2.2}$$

In the case of $BaSnO_3$, the constants are expected to be rather high due to a steep energy valley that results from a good match of the ionic sizes of the two cations. Like we discussed at the end of Section 1.1, this is equivalent to saying that the material is relatively stiff. The structure is identical to the ideal cubic structure in Figure 2.1.

$CsPbI_3$ is a halide perovskite. Its primitive unit cell consists of one caesium ion with charge 1+, one lead ion with charge 2+, and three iodine ions with charge 1−. It is often used in the field of optoelectronics [35]. However, stabilizing the cubic phase requires considerable effort due to a low tolerance factor of $t \approx 0.81$. For example, phase stability is often increased by the doping of metals [35]. In addition, halide perovskites generally exhibit weaker bonds than oxide perovskites [36]. The X-anions are larger here, hence their electron density is more diffuse, while in the case of oxygen a more compact density allows the B- and X-ions to be closer together

due to a more efficient shielding of the positively charged nucleus. Also, the iodine has less charge than the oxygen in $BaSnO_3$. The iodine cloud in $CsPbI_3$ is more easily polarizable, while the Sn and O in barium stannate exhibit strong directional covalent bonds [37]. Hence—although the symmetry is the same, thus leading to the same elastic tensor Eq. (2.2)—the energy curve is expected to be more shallow, resulting in lower values of the SOECs (a softer material). The structure of $CsPbI_3$ again is the same as in Figure 2.1.

$LaInO_3$ is an oxide perovskite. The primitive unit cell consists of one lanthanum ion with charge 3+, one indium ion with charge 3+, and three oxygen ions with charge 2−. It crystallizes in the orthorhombic structure because the A-cation is too small to accommodate the cubic structure. This introduces a high amount of anisotropy to the system. The periodicity of the lattice is not the same along the spatial axes. This also transfers to the elastic properties of the crystal: A uniaxial deformation in the x-direction will now not yield the same change in elastic energy as in y-direction anymore, and so forth. The elastic tensor for the orthorhombic crystal system reads as follows [38]:

$$\underline{\underline{C}} = \begin{pmatrix} C_{11} & C_{12} & C_{13} & & & \\ C_{12} & C_{22} & C_{23} & & & \\ C_{13} & C_{23} & C_{33} & & & \\ & & & C_{44} & & \\ & & & & C_{55} & \\ & & & & & C_{66} \end{pmatrix}, \tag{2.3}$$

with 9 independent elastic constants. According to what we found in Section 1.2, this means that we have to compute the changes in energy for 9 different distortions, making the calculation more time-consuming than for the other two materials. The anisotropy also means that the lattice parameter denoting the length of the cell that we use for the computation will now be different in every direction. The structure of $LaInO_3$ can be seen in Figure 2.2. Since the In-ions have a small ionic radius and a high charge of 3+, we expect the bond lengths in the central octahedra to be relatively stiff compared to changes in rotation of the whole octahedron (which keep the bond lengths the same) [39]. This could hint at an elastic tensor with significantly higher values of the SOECs for volume deformations (C_{11}, C_{22}, and C_{33}) than for shear deformations (C_{44}, C_{55}, and C_{66}).

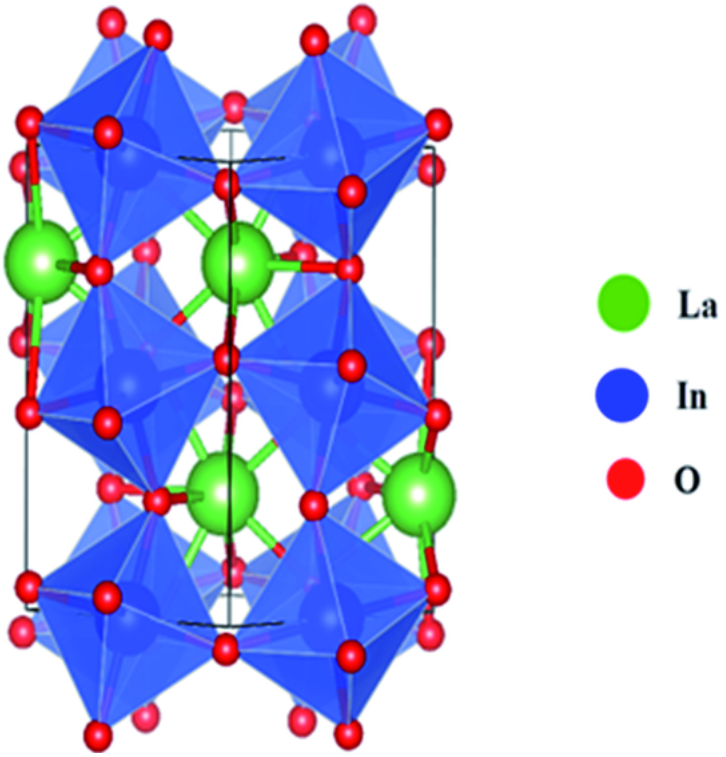

Figure 2.2: The orthorhombic structure of $LaInO_3$. The octahedra of In-O bonds are tilted in order to reach a state of lower energy. The computational cell is significantly bigger than in Figure 2.1 to account for the reduced symmetry. All the lattice parameters for the three spatial directions are different. The image was taken from Ref. [40]

Chapter 3

Method

This chapter describes the method we use to calculate the elastic constants with Kohn-Sham (KS) density-functional theory (DFT). First, the **exciting** package [1] is introduced, a full-potential all-electron implementation of a basis set consisting of linearized augmented plane waves and local orbitals (LAPW+lo). Then the workflow of obtaining the second-order elastic constants (SOECs) is explained. We make use of the **ElaStic** tool [2] for **exciting** here.

3.1 The exciting package

The **exciting** code [1] implements a basis set of specific functions $\psi_i(\underline{r})$ into which the KS states $\phi_i(\underline{r})$ from Section 1.4 can be expanded, according to Eq. (1.44). We construct this basis set one by one. Since we are dealing with a periodic lattice, the index i is abandoned in favor of the band index n and the wave vector $\underline{k}$. For every wave vector $\underline{k}$ in the Brillouin zone of the reciprocal lattice, there are many states with different energies denoted by the band index n. Ideally, this gives a continuous band structure for the whole crystal.[1] The updated KS Eq. (1.32) is:

$$\hat{H}_{\mathrm{KS}}\ \phi_{n,\underline{k}}(\underline{r}) = \varepsilon_{n,\underline{k}}\ \phi_{n,\underline{k}}(\underline{r})\,. \tag{3.1}$$

It can be solved for every $\underline{k}$, yielding a set of KS states $\phi_{n,\underline{k}}(\underline{r})$. To find a new formulation of Eq. (1.44) for a periodic lattice, we use Bloch's theorem [41], which states that wave functions in periodic potentials have to consist of a plane wave $e^{i\underline{k}\cdot\underline{r}}$ modulated with a function $w(\underline{r})$ that has the same periodicity as the crystal lattice:

$$\phi_{n,\underline{k}}(\underline{r}) = e^{i\underline{k}\cdot\underline{r}}\ w_{n,\underline{k}}(\underline{r})\,. \tag{3.2}$$

[1] Look in Ref. [12] for a detailed description of the Bloch theorem and the reciprocal lattice.

Using this form, we can now expand $w_{n,\underline{k}}(\underline{r})$ into a Fourier series, where the sum runs over reciprocal lattice vectors $\underline{G}$, using the Fourier coefficients $c_{\underline{G}}^{n,\underline{k}}$:

$$\phi_{n,\underline{k}}(\underline{r}) = e^{i\underline{k}\cdot\underline{r}} \sum_{\underline{G}} c_{\underline{G}}^{n,\underline{k}}\; e^{i\underline{G}\cdot\underline{r}} = \sum_{\underline{G}} c_{\underline{G}}^{n,\underline{k}}\; e^{i(\underline{G}+\underline{k})\cdot\underline{r}}\,. \tag{3.3}$$

The periodicity of this function can be verified by considering a translation by some direct lattice vector $\underline{R}$. Because of the relation $\underline{G}\cdot\underline{R} = 2\pi m$ ($m \in \mathbb{Z}$) [12], a translation would yield the same function: $e^{i\underline{G}\cdot(\underline{r}+\underline{R})} = e^{i\underline{G}\cdot\underline{r}}\; e^{i\underline{G}\cdot\underline{R}} = e^{i\underline{G}\cdot\underline{r}}$. Equation (3.3) constitutes a basis set consisting of plane waves. The problem with this choice is that the all-electron wave function will show much more oscillations near the strong nuclear potentials than in regions further away from the atoms. The solution proposed by the so-called augmented plane waves (APW) is to split the computational cell of the crystal into two domains: The so-called muffin tin region (MT) consists of spheres that are centered on every atom α. For every different type of atom the muffin tin sphere is defined by the muffin tin radius R_α. The remaining region between the atoms is called the interstitial region (I), in which the wave function will be smoother. Thus it makes sense to describe these two domains with different basis functions. The APW basis set is defined by:

$$\phi_{n,\underline{k}}(\underline{r}) = \sum_{\underline{G}} c_{\underline{G}}^{n,\underline{k}}\; \psi_{\underline{G}+\underline{k}}(\underline{r})\,, \tag{3.4}$$

where $\psi_{\underline{G}+\underline{k}}(\underline{r})$ is different for the MT and I ($r = |\underline{r}|$):

$$\psi_{\underline{G}+\underline{k}}^{\mathrm{APW}}(\underline{r}) = \begin{cases} \sum\limits_{l,m} A_{lm\alpha}^{\underline{G}+\underline{k}}\, u_{l\alpha}(r_\alpha)\, Y_{lm}(\hat{\underline{r}}_\alpha)\,, & r_\alpha \le R_\alpha,\quad \underline{r} \in \mathrm{MT}, \\ \frac{1}{\sqrt{\Omega}}\, e^{i(\underline{G}+\underline{k})\cdot\underline{r}}\,, & \underline{r} \in \mathrm{I}\,. \end{cases} \tag{3.5}$$

In I, we have the same plane waves like in Eq. (3.3), suitable for the smooth behavior. Here Ω is the volume of the unit cell. In the MT though, instead of plane waves, the basis contains atomic orbitals consisting of the radial functions $u_{l\alpha}(r)$ for an atom α and spherical harmonics $Y_{lm}(\hat{\underline{r}})$. The sum runs over the orbital angular momentum quantum numbers l, then over the magnetic quantum numbers $m = -l, ..., l$. The vector $\underline{r}_\alpha$ is centered on the respective atom α, and $\hat{\underline{r}}_\alpha$ is its directional vector, indicating that the arguments of Y are its two angular coordinates. The $A_{lm\alpha}^{\underline{G}+\underline{k}}$ are coefficients that ensure the continuity of $\psi_{\underline{G}+\underline{k}}^{\mathrm{APW}}$ at the boundary of every MT and I. To solve the KS Eq. (3.1) we now need to find these coefficients, $A_{lm\alpha}^{\underline{G}+\underline{k}}$ and $c_{\underline{G}}^{n,\underline{k}}$.

The radial functions are solutions to the radial Schrödinger equation and therefore implicitly depend on the energy eigenvalues themselves: $u_{l\alpha} = u_{l\alpha}(r_\alpha; \varepsilon)$. Looking at our matrix eigenvalue Eq. (1.46), this becomes a problem because $\underline{\underline{H}}$ and $\underline{\underline{S}}$ are

now also dependent on the eigenvalues, since they are expressed in the APW basis: $\underline{\underline{H}}(\varepsilon_i) \cdot \underline{c}_i = \varepsilon_i \, \underline{\underline{S}}(\varepsilon_i) \cdot \underline{c}_i$. This equation is non-linear. On top of the actual self-consistent loop we described at the end of Section 1.4, one would have to iteratively converge every energy eigenvalue at every single step. This would be very numerically expensive. The idea behind the linearized augmented plane waves (LAPW) is to linearize the energy dependence of the radial functions by taking only the first two terms in its Taylor series:

$$u_{l\alpha}(r_\alpha; \varepsilon) = u_{l\alpha}(r_\alpha; \varepsilon_{l\alpha}) + (\varepsilon - \varepsilon_{l\alpha}) \, \dot{u}_{l\alpha}(r_\alpha; \varepsilon_{l\alpha}) \,, \tag{3.6}$$

where $\dot{u}_{l\alpha} = \partial u_{l\alpha} / \partial \varepsilon \,|_{\varepsilon = \varepsilon_{l\alpha}}$. The energy-dependent prefactor of the second term is then absorbed into new coefficients $B_{lm\alpha}^{\underline{G}+\underline{k}}$, removing the energy dependency completely. The new LAPW basis set looks like the following for the MT regions:

$$\psi_{\underline{G}+\underline{k}}^{\mathrm{LAPW}}(\underline{r}) = \sum_{l,m} \left[A_{lm\alpha}^{\underline{G}+\underline{k}} \, u_{l\alpha}(r_\alpha; \varepsilon_{l\alpha}) + B_{lm\alpha}^{\underline{G}+\underline{k}} \, \dot{u}_{l\alpha}(r_\alpha; \varepsilon_{l\alpha}) \right] Y_{lm}(\hat{\underline{r}}_\alpha) \,. \tag{3.7}$$

This approximation is only good for states near $\varepsilon_{l\alpha}$. The addition of local orbitals (LAPW+lo) improves the accuracy for a wider range of energies by adding more degrees of freedom in the expansion for the MT regions. Everywhere else the local orbital basis functions vanish [1]:

$$\psi_\mu^{\mathrm{lo}}(\underline{r}) = \begin{cases} \delta_{\alpha,\alpha_\mu} \delta_{l,l_\mu} \delta_{m,m_\mu} \left[a_\mu u_{l\alpha}(r_\alpha; \varepsilon_{l\alpha}) + b_\mu \dot{u}_{l\alpha}(r_\alpha; \varepsilon_{l\alpha}) \right] Y_{lm}(\hat{r}_\alpha), & r_\alpha \leq R_\alpha, \\ 0 \,, & \underline{r} \in \mathrm{I} \,. \end{cases} \tag{3.8}$$

Again, the coefficients a_μ and b_μ ensure continuity at the MT boundaries and that every $\psi_\mu^{\mathrm{lo}}(\underline{r})$ is normalized to 1. The local orbitals are specific for each atom α and each channel (l, m). Due to the orthogonality of spherical harmonics [42], the different local orbitals are also orthogonal to each other.

With this, we have now constructed the complete LAPW+lo basis set:

$$\phi_{n,\underline{k}}(\underline{r}) = \sum_{\underline{G}} c_{\underline{G}}^{n,\underline{k}} \; \psi_{\underline{G}+\underline{k}}^{\mathrm{LAPW}}(\underline{r}) \;\; + \;\; \sum_\mu c_\mu^n \; \psi_\mu^{\mathrm{lo}}(\underline{r}) \,. \tag{3.9}$$

Due to their locality, the coefficients that belong to the expansion of local orbitals, c_μ^n, don't depend on $\underline{k}$.

To monitor the accuracy of this basis set and with it the overall computational effort, **exciting** allows us to choose certain cutoff parameters as an input which restrict the size of the basis set. These are explained in the following:

- **ngridk**: This discretizes the first Brillouin zone of the reciprocal lattice into a cubic mesh of $\underline{k}$-points. For every zone in the mesh, Eq. (3.1) is solved for a

single vector $\underline{k}$. Like this, we don't have to solve it for all the (infinitely many and not countable) $\underline{k}$ in the Brillouin zone, which makes it a very important parameter to control the complexity of the calculation [43]. `ngridk` is also important when the electron density in Eq. (1.35) is computed [44] using the KS states. Technically, this needs to be done using an integral over the Brillouin zone [45]:

$$n(\underline{r}) = \sum_n \int_{BZ} \frac{\mathrm{d}^3 k}{2\pi^3} \; f_n(\underline{k}) \, |\phi_{n,\underline{k}}(\underline{r})|^2 \,, \tag{3.10}$$

where we sum over all the occupied energy bands n, weighted by a distribution function $f_n(\underline{k})$ which models the occupancy of states across the $\underline{k}$-space. By sampling the $\underline{k}$-space into a grid, this degenerates into the sum:

$$n(\underline{r}) \approx \sum_{n,\underline{k}} w_{\underline{k}} \; f_{n,\underline{k}} \; |\phi_{n,\underline{k}}(\underline{r})|^2 \,, \tag{3.11}$$

running over n and a set of now fixed $\underline{k}$-points, weighted by $w_{\underline{k}}$.[2] This simplification applies to any integral that needs to be evaluated over the $\underline{k}$-space. If the unit cell of the direct lattice is big and includes many atoms—like it was the case with $LaInO_3$ for example—then the Brillouin zone of the reciprocal lattice (the Fourier transform of the direct lattice) is small, meaning we need less $\underline{k}$-points to achieve the same accuracy.

- **`rgkmax`**: This is the cutoff parameter for the plane wave expansion in Eq. (3.5) and determines how many plane waves in I are included. It is defined as $\texttt{rgkmax} = |\underline{G} + \underline{k}|_{\max} \cdot R_\alpha$ [44]. The muffin tin radii R_α are included here because of the continuous matching at the MT boundary: Should they be too small, one would need a higher resolution in the I to portray the more frequent changes in the wave function near the atoms, meaning more terms in the $\underline{G}$ expansion. This is why R_α is coupled with the plane wave cutoff in `rgkmax`. The parameter should also be connected to the choice of the amount of (l, m) channels in the LAPW expansion in Eq. (3.7), which is defined in the so-called species files for the atoms (an example can be seen in Appendix A). `rgkmax` needs to be high enough to match the resolution inside the MT. However, increasing it comes with high computational cost as the runtime scales roughly to the power of 9 with it [29].

- **`gmaxvr`**: In I, the external potential $V(\underline{r})$, the density $n(\underline{r})$, and other quantities are expanded into a Fourier series, limited by the cutoff parameter

[2] If it is an even sampling, then all weights contribute the same portion to the result. It holds that $\sum_{\underline{k}} w_{\underline{k}} = 1$

$|G|_{\max} =$ `gmaxvr`. This parameter becomes important for functionals beyond the LDA, since they take into account ∇n and thus need a higher resolution of the electron density.

- **`rmt`**: The MT radii R_α are specified with this parameter for every type of atom in the computational cell. As mentioned above, should they be too small, the calculation becomes unnecessarily expensive. Should they be too large though, the different MT regions could overlap with each other for certain deformations of the cell, terminating the calculation.

3.2 The `ElaStic` workflow

Before calculating the energy of deformed unit cells to describe the elastic behavior of the perovskites, we need to find the exact size of the unit cell when no stress is applied. In other words, the lattice parameter a of the cell in equilibrium—or the lattice parameters a, b, and c for the anisotropic $LaInO_3$. In the case of the cubic materials this is done by performing **`exciting`** calculations for a series of isotropic volume deformations, then fitting the behavior with the Birch-Murnaghan equation of state (BM-EOS) [9]:

$$E(V) = E_0 + \frac{9V_0B}{16}\left\{\left[\left(\frac{V_0}{V}\right)^{\frac{2}{3}} - 1\right]^3 B' + \left[\left(\frac{V_0}{V}\right)^{\frac{2}{3}} - 1\right]^2 \left[6 - 4\left(\frac{V_0}{V}\right)^{\frac{2}{3}}\right]\right\}, \quad (3.12)$$

where E_0 and V_0 denote the equilibrium energy and volume, respectively, and B is the bulk modulus (describing the elastic response under hydrostatic pressure). $B' = \partial B/\partial p\,|_{p=0}$ is the derivative of the bulk modulus with respect to the pressure p. This value is not necessary in our description of linear elasticity, yet in the BM-EOS it is taken as a fit parameter to obtain the right values for V_0 and B.

For the orthorhombic perovskite $LaInO_3$ we have to perform individual fits for the volume and the relations of the lattice parameters b/a and c/a, because all three parameters are different here and have to be relaxed independent of each other. The volume fits were also done using the BM-EOS, for the ratios 4th order polynomial fits were used. An example for this process can be found in Table 3.1. As a last step, we also have to do internal relaxations of the relative atomic positions in the unit cell, since the complex crystal structure of $LaInO_3$ shifts the equilibrium positions of each atom for every distortion of the whole unit cell.[3]

[3]This was done iteratively by minimizing the residual forces [46] for each nucleus, using the respective exchange-correlation functional. For the optimization the Broyden–Fletcher–Goldfarb–Shanno algorithm [47] was used. When not successful, we switched to

Table 3.1: Example for a structural relaxation of the $LaInO_3$ unit cell. An external optimization of the equilibrium cell was performed in 5 steps, alternating between isotropic volume deformations and anisotropic deformations isolating the behavior when changing single lattice parameters. In the final step an internal relaxation of nuclear positions was performed (with a fixed unit cell). This example calculation was done using the LDA functional, the lattice parameters are given in Angstrom. To showcase the convergent behavior, four decimal places are included. The starting values are taken from Ref. [49]. The following set of input parameters was chosen: `rgkmax` = 8, `ngridk` = 4×3×4, and `gmaxvr` = 18.

Step	**Opt. value**	a	b	c
0		5.9506	8.2159	5.7075
1	V	5.9031	8.1503	5.6620
2	b/a	5.9051	8.1447	5.6639
3	V	5.9050	8.1446	5.6638
4	c/a	5.9046	8.1440	5.6646
5	V	5.9046	8.1440	5.6646

When the equilibrium structures are obtained, the elastic deformation calculations can begin. For every crystal structure, the `ElaStic` tool [2] generates a series of deformations in Lagrangian strain. The associated Lagrangian strain vectors in Voigt notation for the cubic structure can be seen in Table 3.2, for the orthorhombic structure in Table 3.3.

Table 3.2: The components of the Lagrangian strain vector $\underline{\eta}$ for the distortion types that `ElaStic` generates for a **cubic** crystal structure. The value of η is specified by the user. 3 linearly independent elastic constants demand 3 different distortion types.

Distortion	η_1	η_2	η_3	η_4	η_5	η_6
`Dst01`	η	η	η	0	0	0
`Dst02`	η	η	0	0	0	0
`Dst03`	0	0	0	2η	2η	2η

the harmonic method [48]. A full description of the underlying theory would be beyond the scope of this work. Look in Ref. [11] for an overview of internal structural relaxation.

Table 3.3: The components of the Lagrangian strain vector $\underline{\eta}$ for the distortion types that `ElaStic` generates for an **orthorhombic** crystal structure. The value for η is specified by the user. 9 linearly independent elastic constants demand 9 different distortion types.

Distortion	η_1	η_2	η_3	η_4	η_5	η_6
`Dst01`	η	η	η	0	0	0
`Dst02`	$0.5\,\eta$	$0.5\,\eta$	$-\eta$	0	0	0
`Dst03`	$0.5\,\eta$	$-\eta$	$0.5\,\eta$	0	0	0
`Dst04`	η	$-\eta$	0	0	0	0
`Dst05`	0	η	0	0	0	0
`Dst06`	0	0	η	0	0	0
`Dst07`	0	0	0	$2\,\eta$	0	0
`Dst08`	0	0	0	0	$2\,\eta$	0
`Dst09`	0	0	0	0	0	$2\,\eta$

As an input, the maximum Lagrangian strain $\eta_{\max}$ and the number of distorted structures that are evenly distributed along the interval defined by $[-\eta_{\max}; \eta_{\max}]$ are given. In this work, standard choices are $\eta_{\max} = 0.05$ with 11 (or 21) distorted structures. Like this, the single η steps are located at clearly recognizable values: 0.01, 0.02, and so on.

Now **`exciting`** converges the ground-state energies for every configuration in the different distortions. After the self-consistent cycle is completed, an internal relaxation of atomic positions is executed, if the crystal structure allows for it. This is often the case in the `Dst03` for cubic materials. Here, a shear strain is applied to the unit cell, which again allows for a relaxation of the atom along the axis of the strain. For the complex structure of $LaInO_3$, a relaxation of the nuclei is possible for every single deformation step in every distortion. Because this internal relaxation is not implemented for hybrid functionals in **`exciting`** yet, the relaxed geometries obtained using the PBE functional were used as the atomic positions for the PBE0 and HSE functionals. This is the coherent choice because, referring to Eqs. (1.42) and (1.43), the basis that these functionals are built upon is the PBE. These relaxations will apply a final correction to the elastic energies.

These energy values then describe the elastic behavior around the energy minimum in equilibrium. An example can be seen in Figure 3.1. To find the curvatures of these energy curves, which can be used to compute the SOECs like we discussed in Section 1.2, `ElaStic` employs polynomial fits of different orders to the data points.

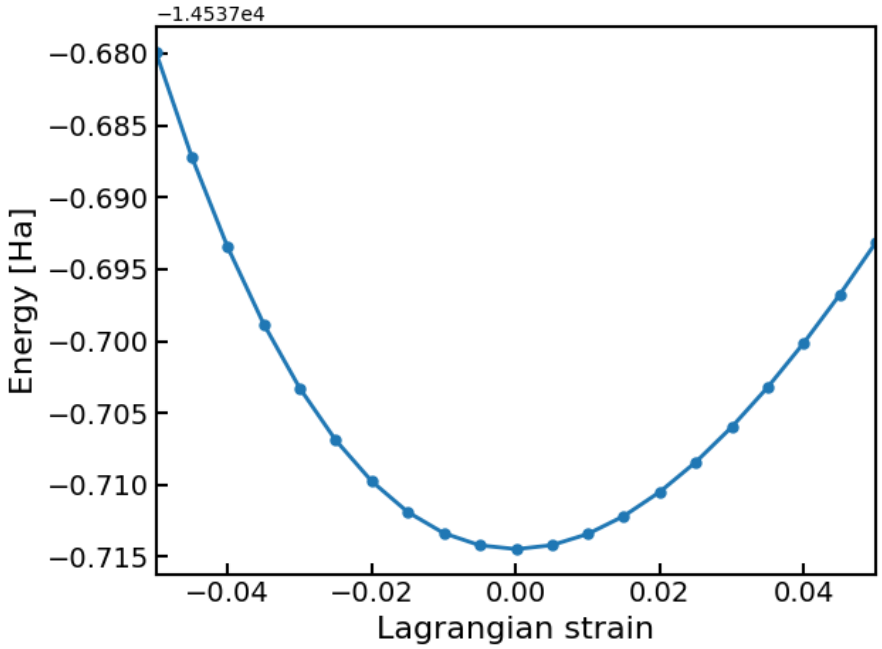

Figure 3.1: Energy in Hartree for different Lagrangian strains. This example shows `Dst01` for $BaSnO_3$ with the PBEsol functional, $\eta_{max} = 0.05$, and 21 data points. If the minimum of the curve is located at zero strain, then the structural optimization was done correctly.

Here, lower-order polynomials may only represent a small amount of data points with sufficient precision, while higher-order polynomials carry the risk of mistaking statistical noise for physics due to their higher degrees of freedom. Hence, **ElaStic** chooses to perform fits with polynomials of orders $n = 2, 4$, and 6, so that one can choose the fit that approximates the data best.[4] Starting from zero Lagrangian strain, the data points from increasing symmetric ranges of strain around $\underline{\eta} = 0$ are used to perform the fits. The results are then shown in a plot with the respective values for the second-order energy derivatives, see Figure 3.2. The second-order polynomial only needs 3 data points for a fit, which is why the results corresponding to these fits start at the $\eta = 0.005$ range. 4th- and 6-th order polynomials start at $\eta = 0.010$ and $\eta = 0.015$, respectively. With an increasing amount of data points, the polynomials will become overdetermined and fail to show convergent results, as it is the case for $n = 2$ early on already. On the other hand, with too few data points, noise dominates the fit parameters instead of the energy curvature. Inbetween those cases there is a region where the results of the fits show a so-called plateau. This plateau region is identified by the user who then chooses a specific polynomial order

[4]This choice of the orders depends on the order of the elastic constants one is computing. For the third-order elastic constants, **ElaStic** would perform fits of orders $n = 3, 5, 7$ and so on [2].

and η value to proceed with the calculation. Having done that for each distortion, `ElaStic` sets up a system of linear equations according to Section 1.2, solves it and gives the resulting elastic constants of the second order inside the elastic tensor and the elastic moduli as an output file.

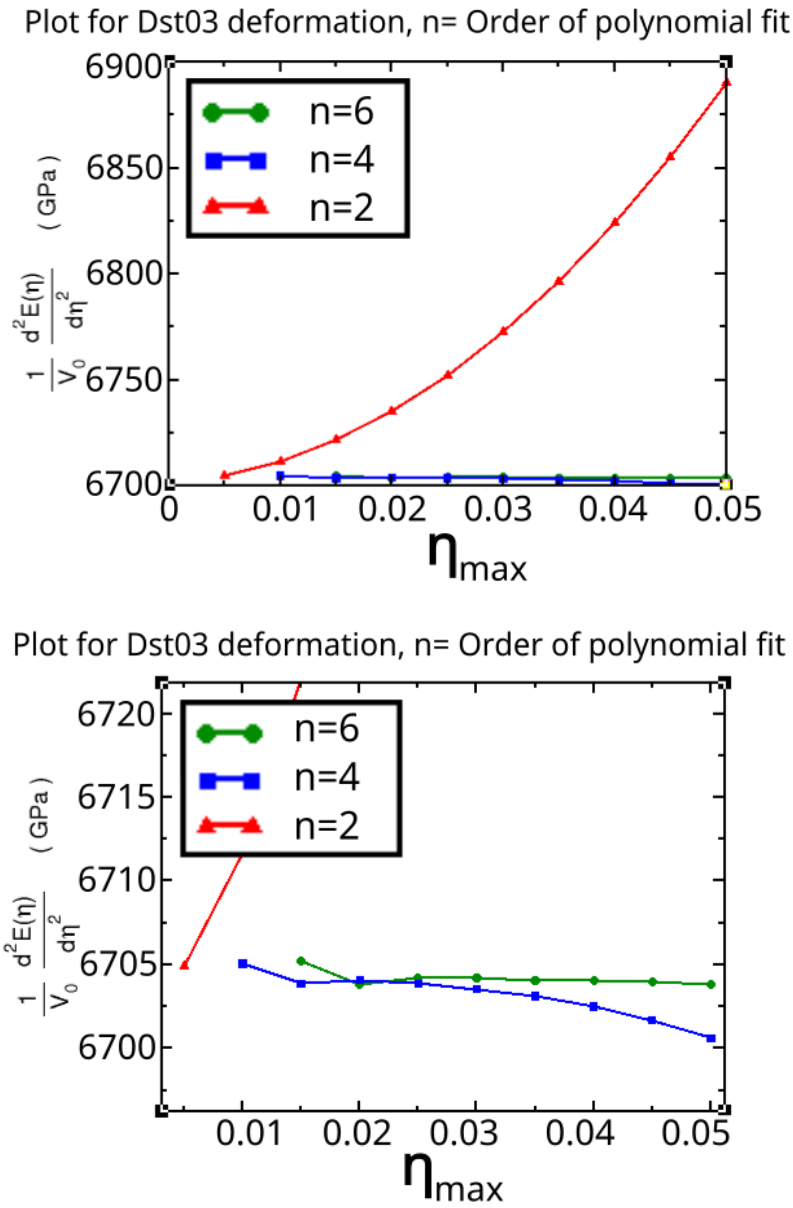

Figure 3.2: The second-order energy derivatives of the energy curve in GPa for different polynomial fits: $n = 2$ in red, $n = 4$ in blue, $n = 6$ in green. Below is a magnification of the plot shown above. This example shows `Dst03` for diamond with the PBE functional, $\eta_{\max} = 0.05$, and 21 data points.

Chapter 4

Results

In this chapter, the results for the lattice parameters and the elastic constants for the three perovskite materials are presented. Also, the values for the Voigt bulk modulus B (describing hydrostatic pressure), the Voigt shear modulus G (describing shear strain), and the Voigt Young modulus Y (describing uniaxial stress) are shown. The respective exchange-correlation functionals used to obtain the results are specified. We also show theoretical and experimental values obtained by other authors to compare the results in this thesis to, if available. The column "Type" names the used exchange-correlation functional. The column "Code/Exp." either specifies with "Exp." that this value has been found with experiments or, for theoretical studies, names the code that was used—if this information was available in the sources. Other codes used in the references include: VASP [50], CASTEP [51], FHI-aims [52], CRYSTAL14 [53], WIEN2k [54], ABINIT [55], and Quantum Espresso [56] (QE). All results are given in either Angstrom for lattice parameters or Gigapascal (GPa) for elastic constants. At the end, the results are discussed: We analyze the contents of the elastic tensors, how the materials compare to each other, and how the exchange-correlation functionals differ.

Convergence calculations can be found in Appendix C. Also, reference calculations for diamond were made with all exchange-correlation functionals, these can be found in Appendix D. In the discussion, these results are used for comparison.

The elastic calculations of $LaInO_3$ for the two hybrid functionals PBE0 and HSE could not be completed within this thesis due to convergence issues in the second-order energy derivatives. The hybrids are a very expensive choice for $LaInO_3$, having significantly more atoms in the unit cell than the other two perovskites. Most likely, the convergence issues could be fixed by increasing the parameter `ngridk`. A $\underline{k}$-point sampling of 4×3×4 was used for $LaInO_3$ with LDA, PBE, and PBEsol and provided sufficiently well converged results. The sampling 3×2×3 of the Brillouin

zone proves to be a too crude approximation in test calculations with these three functionals. Changing from a 3×2×3-grid to a higher-resolution grid of 4×3×4 leads to an increase in computation time in a ratio of 18 to 48. Due to time limitations we had to opt for 3×2×3 in the case of hybrids, them already being highly expensive. Although with this choice the bulk moduli were converged within a range of 1.5%, the `ElaStic` studies did not produce polynomial fits that were sufficiently well converged. We expect to complete the study of $LaInO_3$ after the completion of this thesis though.

4.1 Barium stannate ($BaSnO_3$)

The equilibrium lattice parameters for cubic $BaSnO_3$ can be found in Table 4.1. The computed elastic constants are presented in Table 4.2, the associated elastic moduli in Table 4.3. Previous theoretical and experimental results are shown below our results in the tables. Ref. [57] from Table 4.3 used ionic charge theory to theoretically predict the bulk modulus, this is indicated by "Estimate" in the column "Code/Exp.". This also applies to Table 4.6 for the next material $CsPbI_3$. For the computationally less expensive functionals LDA, PBE, and PBEsol a set of relatively high input parameters was used: **rgkmax** = 9, **ngridk** = 14×14×14, and **gmaxvr** = 25 (18 for LDA). For the more expensive hybrid functionals PBE0 and HSE the following set was used: **rgkmax** = 8, **ngridk** = 6×6×6, and **gmaxvr** = 25.

Table 4.1: Lattice parameters for $BaSnO_3$. All results are given in Angstrom.

Reference	Code/Exp.	Type	a
This work	**exciting**	LDA	4.090
		PBE	4.183
		PBEsol	4.129
		PBE0	4.115
		HSE	4.116
Moreira *et al.* [58]	CASTEP	LDA	4.055
		PBE	4.142
Bouhemadou and Haddadi [59]	CASTEP	LDA	4.059
		PBE	4.1916
Zupancic *et al.* [60]	FHI-aims	PBEsol	4.119
Mat. Project [61]	VASP	PBE	4.189
Wang *et al.* [62]	VASP	PBE	4.186
		HSE	4.129
Scanlon [63]	VASP	HSE	4.13
		PBE0	4.13
Mountstevens *et al.* [64]	Exp.		4.1151
Maekawa *et al.* [65]	Exp.		4.116
Prodjosantoso *et al.* [66]	Exp.		4.1168

Table 4.2: Elastic constants for $BaSnO_3$. All results are given in GPa.

Reference	Code/Exp.	Type	C_{11}	C_{12}	C_{44}
This work	**exciting**	LDA	303.2	92.3	98.9
		PBE	245.5	76.7	88.9
		PBEsol	278.0	85.0	93.8
		PBE0	294.4	99.1	100.7
		HSE	289.3	99.2	101.0
Bouhem. and Had. [59]	CASTEP	LDA	358.5	93.5	110.3
		PBE	285.2	68.5	84.3
Moreira *et al.* [58]	CASTEP	PBE	251	82.3	98.1
De Jong *et al.* [67]	VASP	PBE	250	76	92
Zupancic *et al.* [60]	FHI-aims	PBEsol	286.5	83.4	93.6
Duarte *et al.* [68]	CRYSTAL14	PBE0	296.33	89.13	111.07
Guendouz *et al.* [69]	WIEN2k	mBJ-GGA	261.4	85.75	87.38

Table 4.3: Elastic moduli for $BaSnO_3$: Bulk modulus B, shear modulus G, and Young modulus Y. All results are given in GPa. "Estimate" means that a theoretical prediction was made based on ionic charge theory, see Ref. [57]. An (*) indicates that the moduli were not mentioned explicitly in the respective reference, but computed here using the elastic constants from the reference.

Reference	Code/Exp.	Type	B	G	Y
This work	**exciting**	LDA	162.6	101.5	252.1
		PBE	133.0	87.1	214.4
		PBEsol	149.4	94.9	235.0
		PBE0	164.2	99.5	248.3
		HSE	162.6	98.6	246.1
Bouhem. and Had. [59]	CASTEP	LDA	181.96	118.7	292.4
		PBE	140.7	93.2	229.1
Moreira *et al.* [58]	CASTEP	PBE	138.5*	92.6*	227.2*
Bévillon *et al.* [70]	ABINIT	PBE		84	207
De Jong *et al.* [67]	VASP	PBE	134	90	221*
Zupancic *et al.* [60]	FHI-aims	PBEsol	151.1*	96.8*	239.3*
Duarte *et al.* [68]	CRYSTAL14	PBE0	158.20	108.08*	264.10*
Guendouz *et al.* [69]	WIEN2k	mBJ-GGA	144.6	87.55	218.47
Verma and Kumar [57]	Estimate		150.9		
Maekawa *et al.* [65]	Exp.		145.8	99.9	244

4.2 Caesium lead iodide ($CsPbI_3$)

The lattice parameters for cubic $CsPbI_3$ can be seen in Table 4.4. The elastic constants are shown in Table 4.5, the elastic moduli in Table 4.6—below the respective previous theoretical and experimental results, if available. For the LDA, PBE, and PBEsol the following set of input parameters was used: **rgkmax** = 9, **ngridk** = 14×14×14, and **gmaxvr** = 25 (18 for LDA). For PBE0 and HSE the following set was used: **rgkmax** = 8, **ngridk** = 6×6×6, and **gmaxvr** = 25.

Table 4.4: Lattice parameters for $CsPbI_3$. All results are given in Angstrom.

Reference	Code/Exp.	Type	a
This work	**exciting**	LDA	6.195
		PBE	6.451
		PBEsol	6.301
		PBE0	6.315
		HSE	6.312
Murtaza and Ahmad [71]	WIEN2k	LDA	6.18
Chang and Park [72]	-	LDA	6.05
Afsari *et al.* [73]	WIEN2k	LDA	6.14
		PBE	6.4011
		PBEsol	6.25
Mat. Project [74]	VASP	PBE	6.414
Aktary *et al.* [75]	CASTEP	PBE	6.432
Zaidi *et al.* [76]	CASTEP	PBE	6.515
Alruqi and Ongwen [77]	QE	PBE	6.391
Idrissi *et al.* [78]	QE	PBEsol	6.28
Ghaithan *et al.* [79]	WIEN2k	PBEsol	6.262
Trots and Myagkota [80]	Exp.		6.28940
Yuan *et al.* [81]	Exp.		6.33
Marronnier *et al.* [82]	Exp.		6.297
Eperon *et al.* [83]	Exp.		6.1769

Table 4.5: Elastic constants for $CsPbI_3$. All results are given in GPa.

Reference	Code/Exp.	Type	C_{11}	C_{12}	C_{44}
This work	**exciting**	LDA	47.0	6.0	3.4
		PBE	31.4	5.2	3.5
		PBEsol	39.1	5.2	3.4
		PBE0	43.0	5.7	4.1
		HSE	42.3	5.4	4.1
Afsari *et al.* [73]	WIEN2k	PBE	34.405	4.709	3.848
Aktary *et al.* [75]	CASTEP	PBE	39.323	6.754	5.352
Roknuzzaman *et al.* [84]	CASTEP	PBE	34.23	4.46	3.24
Zaidi *et al.* [76]	CASTEP	PBE	47.90	7.94	4.84
Fadla *et al.* [85]	CASTEP	PBE	35.51	5.09	4.11
Koshi *et al.* [86]	VASP	PBE	34.84	4.73	3.66

Table 4.6: Elastic moduli for $CsPbI_3$: Bulk modulus B, shear modulus G, and Young modulus Y. All results are given in GPa. "Estimate" means that a theoretical prediction was made based on ionic charge theory, see Ref. [57]. An (*) indicates that the moduli were not mentioned explicitly in the respective reference, but computed here using the elastic constants from the reference.

Reference	Code/Exp.	Type	B	G	Y
This work	**exciting**	LDA	19.6	10.2	26.1
		PBE	13.9	7.3	18.7
		PBEsol	16.5	8.8	22.5
		PBE0	18.1	9.9	25.2
		HSE	17.7	9.9	25.0
Murtaza and Ahmad [71]	WIEN2k	LDA	19.8		
Jin *et al.* [87]	-	LDA	19.88		
Afsari *et al.* [73]	WIEN2k	LDA	20.22		
		PBE	14.608	6.858	17.79
		PBEsol	16.91		
Alruqi and Ongwen [77]	QE	PBE	14.51	6.57	17.04
Aktary *et al.* [75]	CASTEP	PBE	17.61	8.522	22.015
Roknuzzaman *et al.* [84]	CASTEP	PBE	14.38	6.30	14.49
Zaidi *et al.* [76]	CASTEP	PBE	21.26*	10.90*	27.93*
Fadla *et al.* [85]	CASTEP	PBE	15.23	8.55	21.61
Koshi *et al.* [86]	VASP	PBE	14.76	8.22*	20.80*
Ghaithan *et al.* [79]	WIEN2k	PBEsol	17.85		
Verma and Kumar [57]	Estimate		16.5		
Rakita *et al.* [88]	Exp.		19.8	7.9	20.1

4.3 Lanthanum indium oxide ($LaInO_3$)

The lattice parameters for orthorhombic $LaInO_3$ can be seen in Table 4.7. The elastic constants are shown in Table 4.8, the elastic moduli in Table 4.9—below the respective previous theoretical and experimental results, if available. Unfortunately, not many references could be found for $LaInO_3$. The following set of input parameters was used: **rgkmax** = 8, **ngridk** = 4×3×4, and **gmaxvr** = 25 (18 for LDA).

In Ref. [89], we suspect a discrepancy for the elastic constants in Table 4.8: In the original reference, the constants C_{55} and C_{66} are exchanged. This presumably is a mistake, since $C_{66} > C_{55}$ for other references and in every calculation of this work as well. Also, Zupancic *et al.* [60] make the same choice and exchange the two values by Erkişi *et al.* [89].

Table 4.7: Lattice parameters for $LaInO_3$. All results are given in Angstrom.

Reference	Code/Exp.	Type	a	b	c
This work	**exciting**	LDA	5.905	8.144	5.665
		PBE	6.020	8.362	5.781
		PBEsol	5.954	8.235	5.712
		PBE0	5.950	8.196	5.721
		HSE	5.955	8.199	5.705
Erkişi *et al.* [89]	VASP	PBE	6.069	8.394	5.814
Mat. Project [90]	VASP	PBE	6.009	8.352	5.771
Zupancic *et al.* [60]	FHI-aims	PBEsol	5.939	8.210	5.698
Ubic and Subodh [91]	Exp.		5.914	8.207	5.723
Jang *et al.* [92]	Exp.		5.9414	8.2192	5.7249
Park *et al.* [93]	Exp.		5.9404	8.2158	5.7229

Table 4.8: Elastic constants for $LaInO_3$. All results are given in GPa. Agreements of Ref. [89] with PBEsol are significantly better than with PBE, however it is stated there that PBE was used.

Reference	Code/Exp.	Type	C_{11}	C_{22}	C_{33}	C_{12}	C_{13}
This work	**exciting**	LDA	252.4	221.4	244.1	126.8	137.7
		PBE	220.3	175.0	216.5	103.8	108.8
		PBEsol	239.1	200.8	230.3	114.7	124.0
Erk. *et al.* [89]	VASP	PBE	238.12	195.28	225.81	111.46	121.69
Zup. *et al.* [60]	FHI-aims	PBEsol	243.9	204.7	234.8	118.8	129.1

Reference	Code/Exp.	Type	C_{23}	C_{44}	C_{55}	C_{66}
This work	**exciting**	LDA	120.8	56.5	61.2	76.3
		PBE	97.6	51.4	50.7	68.2
		PBEsol	111.2	53.9	56.7	72.2
Erkişi *et al.* [89]	VASP	PBE	104.38	52.61	58.90	70.37
Zupancic *et al.* [60]	FHI-aims	PBEsol	112.2	54.7	58.1	73.6

Table 4.9: Elastic moduli for $LaInO_3$: Bulk modulus B, shear modulus G, and Young modulus Y. All results are given in GPa. An (*) indicates that the moduli were not mentioned explicitly in the respective reference, but computed here using the elastic constants from the reference.

Reference	Code/Exp.	Type	B	G	Y
This work	**exciting**	LDA	165.4	61.0	162.9
		PBE	136.9	54.2	143.6
		PBEsol	152.2	57.9	154.2
Erkişi *et al.* [89]	VASP	PBE	147.25	57.38	152.36
Zupancic *et al.* [60]	FHI-aims	PBEsol	156.0*	58.8*	156.7*

4.4 Discussion

Overall, the calculated values are in good agreement with previous works. The three structures are mechanically stable since all of the computed elastic constants satisfy the Born elastic stability criteria [94]. A first look at the data shows that larger lattice parameters a tend to correspond to smaller elastic constants, reflecting weaker bonding. A smaller unit cell, on the other hand, often indicates stronger bonds between the atoms and thus a stiffer material.

Looking at our three perovskite materials, firstly irrespective of the differences in the exchange-correlation functionals, we can confirm the predictions made in Chapter 2: $BaSnO_3$ is found to have high elastic constants in the elastic tensor compared to the other two materials. Its three identical diagonal components C_{11}, C_{22}, and C_{33} corresponding to volume deformations lie in a range of 246 to 303 GPa, indicating a steep energy valley for elastic distortions. Values for the bulk modulus B range from 133 to 164 GPa. Still, this is only one third of B for bulk diamond, the hardest known crystal structure, see Appendix D. The identical constants C_{44}, C_{55}, and C_{66} describing the elastic response for shear distortions range from 89 to 101 GPa and are of similar magnitude to the identical off-diagonal coupling components C_{12}, C_{23}, and C_{13}. These ranges are in good agreement with the literature and very similar to those of other oxide perovskites in the cubic crystal structure [95].

$CsPbI_3$ is shown by the results to have the softest lattice of the three perovskites. Values for C_{11} range from 31 to 47 GPa and values for B from 14 to 20 GPa. Different directions of strain are only weakly coupled with a C_{12} of 5 to 6 GPa. Given the low magnitude of the values, C_{44} still is significantly lower than C_{11} with a range of 3 to 4 GPa. Compared to $BaSnO_3$, these low values indicate the phase instability of cubic $CsPbI_3$: A tilt or rotation of the central octahedron in the unit cell could shift the phase to the orthorhombic crystal structure. The values for the bulk modulus and the elastic constants can be compared very well to other halide perovskites [96], known to be soft materials, as discussed in Chapter 2.

The high anisotropy of the orthorhombic $LaInO_3$ leads to the larger set of nine independent constants in the elastic tensor. However, they can still be split into three groups of constants with similar magnitudes: The diagonal components in the upper-left C_{11}, C_{22}, and C_{33} with a range of 175 to 252 GPa almost reach the respective values in the tensor for $BaSnO_3$. The smallest of these clearly is C_{22}, meaning that the material is softest in the axis of lattice parameter b which is by far the largest lattice constant in unit cell calculations.[1] The anisotropic bonding

[1]Note that, when looking at other references, one always has to verify if the lattice parameters a, b, and c are chosen to be the same. If this is not the case, then the elastic constants in the

along the b direction, where the lattice symmetry repeats less frequently, allows for more structural flexibility and thus exhibits a softer elasticity in this case. The values for C_{12}, C_{23}, and C_{13} lie in a group of constants that range from 98 to 138 GPa. The diagonal entries in the lower-right C_{44}, C_{55}, and C_{66} range from 51 to 76 GPa. Unlike for $BaSnO_3$—where C_{44} and C_{12} were of similar magnitude—this suggests a relatively soft elastic response for shear deformations in $LaInO_3$. It also shows when looking at the shear modulus G, which ranges from 54 to 61 GPa: This is low relative to the bulk modulus B, compared to the moduli of the other perovskites. This confirms our predictions from Chapter 2: Because of the strong bonds in the BX_6 octahedron the structure resists volume deformations more than shear deformations. Unfortunately, no experimental references could be found for the elastic properties of $LaInO_3$.

Now we compare the exchange-correlation functionals based on their results. In our data, for all lattice parameters the LDA yields the smallest value and the PBE functional yields the largest value. This is well known from previous theory [97]: LDA, based on the homogeneous electron density, overestimates the negative exchange energy, as it does not take into account the variation of the electron density, which will be higher and more fluctuating near the cores and significantly lower in the interstitial regions. Hence, it predicts stronger bonds and underestimates the lattice constant. For every investigated material in this work, the LDA results are around 1% below the experimental reference values. The GGA functionals try to compensate this error by taking into account the gradient of the density, as discussed in Section 1.5. However, the PBE is known to overcompensate and tends to predict bonds that are too weak [97], thus overestimating the lattice parameter. Here, the PBE lattice constants lie 1% to 2% above the experiments. It can be said that the LDA and PBE function as lower and upper bounds for the true lattice parameter. This behavior of the two functionals replicates for the elastic properties, only vice versa: Coinciding with the fact that smaller lattice parameters tend to produce larger elastic constants, all the elastic results have the largest values for the LDA. The lower bound here is the PBE, showing the smallest values. With one exception (the bulk modulus for $CsPbI_3$ by Rakita *et al.* [88]) the experimental elastic moduli lie between the LDA and PBE predictions.

PBEsol tries to improve the equilibrium properties of the PBE functional for solids [24]. Indeed, for every single calculation, be it lattice or elastic constant, the values obtained with PBEsol lie between the LDA and PBE, often right in the middle. Lattice parameters with PBEsol are very close to the experimental findings for all three perovskites, exhibiting an agreement within 0.2% to 0.4% of the

tensor will change positions in the same manner.

experimental consensus. There were no available experiments that studied the elastic properties of $LaInO_3$, however, there is a high agreement of the elastic constants and moduli with Zupancic *et al.* [60] who also used the PBEsol functional. This also applies to the same comparison in PBEsol for $BaSnO_3$. Noticeable is also the strikingly high agreement of PBEsol bulk moduli for $BaSnO_3$ and $CsPbI_3$ with the findings of Verma and Kumar [57] who used ionic charge theory to theoretically predict the bulk modulus of cubic perovskites. Overall, the results confirm the better predictions for the structural properties of solids with the optimized PBEsol functional. Considering computation time, PBEsol and PBE are comparable. For $LaInO_3$ they took roughly the same time to converge, while for $CsPbI_3$, PBE reached convergence slightly earlier. Interestingly, the computation time for $BaSnO_3$ using PBEsol was consistently only about one third of the time it took using PBE. To conclude, PBEsol is a reasonable choice to calculate structural properties of solids, it combines high precision with relatively low computational cost—compared to the very expensive hybrids. For shortest waiting time, one can also resort to the LDA, which will produce a good first reference point.

The two hybrid functionals PBE0 and HSE apply further corrections to the calculations by incorporating a portion of exact exchange energy. Overall, they both produce very similar results. For lattice parameters, they deviate from each other by less than 0.1%, except for c of $LaInO_3$ where they deviate by 0.3%. For elastic constants and moduli, they show deviations of 1% to a maximum of 2%. For the investigated materials, the limitation of Hartree Fock exchange to short-range interactions seems to have only a small effect. Although the aim of the HSE is to make computation more efficient by splitting up long- and short-range interactions, thus reducing convergence time, a clear trend in our calculations suggests otherwise for the current implementation in **`exciting`**: The HSE consistently took more time to converge than PBE0. It was less noticeable for $LaInO_3$, which could suggest that the HSE effects only start to pay off for larger unit cells with more atoms. However, different values for α and ω were not tested to further investigate this topic. The trend definitely demands further study. Comparing the values for the lattice constants predicted by the hybrids with the other functionals, we notice that they are close to the PBEsol results, always showing less than 0.5% deviation from them. In the case of $BaSnO_3$, the hybrid lattice constants are a direct match with the experimental findings, improving upon the PBEsol values. However, for $LaInO_3$ and especially $CsPbI_3$ the experimental lattice parameters are too widely spread to be able to make a similar observation. Considering that computation time for hybrids was about ten times higher than for PBEsol, the choice of a hybrid functional to calculate the size of the unit cell has to be well-founded—unless one needs this optimization for further numerical studies with hybrids. For the elastic

constants, PBE0 produces results that are slightly higher than for HSE. In most cases both hybrid functionals yield values between PBEsol and LDA results, generally leaning towards LDA, sometimes even higher than LDA—despite the fact that the respective lattice constants are higher for hybrids than for the LDA in every material. This observation is supported by our test calculations for diamond, see Appendix D. There, C_{11}, C_{44}, and all elastic moduli exceed the LDA values, while at the same time the lattice constant a is also higher. This is verified by the given literature. A source of error might be that the atom positions were not relaxed using the respective hybrid functional but taken from internal relaxations performed with PBE. However, Råsander and Moram [98] were able to relax using hybrids but still come to the same conclusion. Looking at their other investigated materials, one can verify the general trend that PBE0 and HSE predict stiffer materials than most other functionals, often with higher values than even the LDA. This suggests that the incorporation of exact Hartree Fock exchange steepens the energy valley around the equilibrium configuration, hinting at an increased sensitivity of exact exchange energy to structural distortions. Last but not least, this proves that the connection of low lattice parameters to large elastic constants and vice versa is too simple and functions more as a rough guideline.

There were almost no experimental data describing the elasticity of the investigated perovskites available, making it difficult to comment on the physical accuracy of the hybrids compared to other exchange-correlation functionals. Also—apart from Duarte *et al.* [68], who used the package CRYSTAL14 [53] to calculate the elastic properties of $BaSnO_3$ with PBE0—we found no theoretical elasticity studies of the three perovskites that used hybrid functionals. The present work establishes new benchmark data in the research field of first-principles calculations based on density-functional theory and exchange-correlation functionals. In particular, our calculations for $BaSnO_3$ using the HSE, and for $CsPbI_3$ using PBE0 and the HSE, constitute new research results in the field.

Conclusions and Outlook

We successfully calculated the elastic properties of the cubic perovskites $BaSnO_3$ and $CsPbI_3$ and the orthorhombic perovskite $LaInO_3$ using first-principles methods in the framework of Kohn-Sham density-functional theory. We used the **exciting** package [1] with an implementation of the LAPW+lo basis set to perform iterative calculations of the elastic energies for small deformations around an equilibrium lattice. For this, we employed five different exchange-correlation functionals: The LDA, the PBE and PBEsol functionals of the GGA and the PBE0 and HSE hybrid functionals. Then we made use of the **ElaStic** tool [2] to use this data to compute the second-order elastic constants and associated elastic moduli for the three materials. The calculations with PBE0 and HSE for the material $LaInO_3$ could not be performed in this work due to time limitations. However, we have established a framework to continue this research after the completion of the thesis.

The present values are generally in good agreement with the literature, although in some cases not enough previous studies could be found to compare our values to. Especially for hybrid functionals there is very little literature presenting first-principles calculations of elastic constants for perovskites. No previous calculations for $BaSnO_3$ using HSE and for $CsPbI_3$ using PBE0 or HSE were available to us. Hence, this work serves as a benchmark study and its results will be made available on the NOMAD repository [10]. In the future, they can be used for predictions of the elastic behavior of the investigated materials under strain in the domain of linear elasticity and they can serve as reference values for further theoretical research.

The implementations of the hybrid functionals in **exciting** demand further studies, like we discussed in Section 4.4. The internal relaxation of the atom positions in the unit cell by minimization of the forces could be implemented for PBE0 and HSE in **exciting** in the future. Also, possible automations of the workflow in this thesis could be investigated. Part of this endeavor is the thesis by Bächli [99], in which a method is developed to choose the order of the polynomial and maximum Lagrangian strain in the **ElaStic**-diagram in Figure 3.2 with numerical methods instead of by manual selection. Furthermore, the calculations done in this work can be extended to other materials in the time to come.

Bibliography

[1] A. Gulans, S. Kontur, C. Meisenbichler, D. Nabok, P. Pavone, S. Rigamonti, S. Sagmeister, U. Werner, and C. Draxl. exciting: a fullpotential all-electron package implementing density-functional theory and many-body perturbation theory. Journal of Physics: Condensed Matter, 26(36), 2014. http://stacks.iop.org/0953-8984/26/i=36/a=363202.

[2] R. Golesorkhtabar, P. Pavone, J. Spitaler, P. Puschnig, and C. Draxl. ElaStic: A tool for calculating second-order elastic constants from first principles. Computer Physics Communications, 184:1861–1873, 2013. https://doi.org/10.1016/j.cpc.2013.03.010.

[3] J. P. Perdew and K. Schmidt. Jacob's ladder of density functional approximations for the exchange-correlation energy. AIP Conference Proceedings, 577: 1–20, 2001. https://doi.org/10.1063/1.1390175.

[4] J. Tan, Y. Li, and G. Ji. Elastic constants and bulk modulus of semiconductors: Performance of plane-wave pseudopotential and local-density-approximation density functional theory. Computational Materials Science, 58(1):243–247, 2012. https://doi.org/10.1016/j.commatsci.2012.01.013.

[5] G. W. Hastings and D. F. Williams. Mechanical properties of biomaterials. Materials Science, Biology, 1980.

[6] R. M. Hazen. Perovskites. Scientific American Magazine, 258(6), 1988. https://doi.org/10.1038/scientificamerican0688-74.

[7] F. Tayari, S. S. Teixeira, M. P. F. Graca, and K. I. Nassar. A Comprehensive Review of Recent Advances in Perovskite Materials: Electrical, Dielectric, and Magnetic Properties. Inorganics, 13(3):67, 2025. https://doi.org/10.3390/inorganics13030067.

[8] Q. A. Akkerman and L. Manna. What Defines a Halide

Perovskite? ACS Energy Letters, 5(2):604–610, 2020. https://dx.doi.org/10.1021/acsenergylett.0c00039.

[9] F. Birch. Finite Elastic Strain of Cubic Crystals. Physical Review, 71(11): 809–824, 1947. https://doi.org/10.1103/PhysRev.71.809.

[10] NOMAD Laboratory. Nomad repository. `https://nomad-lab.eu/nomad-lab`, accessed: March 30, 2026.

[11] F. Giustino. Materials Modelling using Density Functional Theory. Oxford University Press, 2014.

[12] C. Kittel. Introduction to Solid State Physics. John Wiley & Sons, 1976.

[13] L. D. Landau and E. M. Lifshitz. Theory of Elasticity. Elsevier Butterworth-Heinemann, 1986.

[14] P. Pavone. Lecture: Theoretical Solid State Physics. `https://moodle.hu-berlin.de/course/view.php?id=130189`. Held at Humboldt University Berlin - winter semester 2024/25.

[15] A. P. Sutton. Physics of Elasticity and Crystal Defects. Oxford University Press, 2020.

[16] M. Born and R. Oppenheimer. Zur Quantentheorie der Molekeln. Annalen der Physik, 389(20):457–484, 1927. https://doi.org/10.1002/andp.19273892002.

[17] P. Hohenberg and W. Kohn. Inhomogeneous Electron Gas. Physical Review, 136(3B):B864–B871, 1964. http://dx.doi.org/10.1103/PhysRev.136.B864.

[18] M. Levy. Universal variational functionals of electron densities, first-order density matrices, and natural spin-orbitals and solution of the v-representability problem. Proceedings of the National Academy of Sciences USA, 76(12): 6062–6065, 1979. https://doi.org/10.1073/pnas.76.12.606.

[19] W. Kohn and L. J. Sham. Self-Consistent Equations Including Exchange and Correlation Effects. Physical Review, 140(4A):A1133–A1138, 1965. http://dx.doi.org/10.1103/PhysRev.140.A1133.

[20] W. Pauli. Über den Zusammenhang des Abschlusses der Elektronengruppen im Atom mit der Komplexstruktur der Spektren. Zeitschrift für Physik, 31: 765–783, 1925. https://doi.org/10.1007/BF02980631.

[21] E. Brémond, A. J. Pérez-Jiménez, C. Adamo, and J. C. Sancho-García. Contemporary DFT: learning from traditional and recent trends for the development and assessment of accurate exchange–correlation functionals. Physical Chemistry Chemical Physics, 28:3779–3796, 2026. https://doi.org/10.1039/D5CP03373J.

[22] P. M. W. Gill P. Loos. The uniform electron gas. WIREs Computational Molecular Science, 6:410–429, 2016. https://doi.org/10.1002/wcms.1257.

[23] J. P. Perdew, K. Burke, and M. Ernzerhof. Generalized Gradient Approximation Made Simple. Physical Review Letters, 77(18), 1996. https://doi.org/10.1103/PhysRevLett.77.3865.

[24] J. P. Perdew, A. Ruzsinszky, G. I. Csonka, O. A. Vydrov, G. E. Scuseria, L. A. Constantin, X. Zhou, and K. Burke. Restoring the Density-Gradient Expansion for Exchange in Solids and Surfaces. Physical Review Letters, 100: 136406, 2008. https://doi.org/10.1103/PhysRevLett.100.136406.

[25] D. Rappoport, N. R. M. Crawford, F. Furche, and K. Burke. Approximate Density Functionals: Which Should I Choose? Encyclopedia of Inorganic Chemistry, Computational Inorganic and Bioinorganic Chemistry:159–172, 2009. https://doi.org/10.1002/0470862106.ia615.

[26] J. C. Slater. A Simplification of the Hartree-Fock Method. Physical Review, 81(3):385–390, 1951. https://doi.org/10.1103/PhysRev.81.385.

[27] C. Adamo and V. Barone. Toward reliable density functional methods without adjustable parameters: The PBE0 model. Journal of Chemical Physics, 110 (13):6158–6170, 1999. https://doi.org/10.1063/1.478522.

[28] J. Heyd, G. E. Scuseria, and M. Ernzerhof. Hybrid functionals based on a screened Coulomb potential. Journal of Chemical Physics, 118(18):8207–8215, 2003. https://doi.org/10.1063/1.1564060.

[29] K. Sinha. Electronic Structure of Oxides and Perovskites: A Benchmark Database. Humboldt Universität zu Berlin, 2024.

[30] D. Z. Metin and N. Gaston. Internal and external pressure in cubic perovskites: electronic structure effects and systematic accuracy from first principles. Electronic structure, 1(3), 2019. https://doi.org/10.1088/2516-1075/ab2833.

[31] V. M. Goldschmidt. Die Gesetze der Krystallochemie. Naturwissenschaften, 14:477–485, 1926. https://doi.org/10.1007/BF01507527.

[32] S. Simpson and M. S. Senn. Octahedral Tilting in Perovskite Polytypes. Chemistry of Materials, 37(12):4524–4533, 2025. https://doi.org/10.1021/acs.chemmater.5c01062.

[33] R. H. Mitchell, M. D. Welch, and A. R. Chakhmouradian. Nomenclature of the perovskite supergroup: A hierarchical system of classification based on crystal structure and composition. Mineralogical Magazine, 81(3):411–461, 2017. https://doi.org/10.1180/minmag.2016.080.156.

[34] H. J. Kim, U. Kim, T. H. Kim, H. S. Mun, B. Jeon, K. T. Hong, W. Lee, C. Ju, K. Hoon Kim, and K. Char. High Mobility in a Stable Transparent Perovskite Oxide. Applied Physics Express, 5(6):061102, 2012. https://doi.org/10.1143/APEX.5.061102.

[35] H. M. Helal, Z. K. Heiba, H. Elshimy, S. Yehia, and A. Mourtada Elseman. Tailoring the Microstructure and Optoelectronic Properties of $CsPbI_3$ via Synergistic Potassium Doping and Surface Passivation for High-Efficiency Perovskite Solar Cells. ACS Applied Energy Materials, 8(16):12157–12167, 2025. https://doi.org/10.1021/acsaem.5c01655.

[36] S. I. Seok and T. Guo. Halide perovskite materials and devices. MRS Bulletin, 45:427–430, 2020. https://doi.org/10.1557/mrs.2020.140.

[37] S. Soleimanpour and F. Kanjouri. First principle study of electronic and optical properties of the cubic perovskite $BaSnO_3$. Physica B Condensed Matter, 432:16–20, 2014. https://doi.org/10.1016/j.physb.2013.09.004.

[38] F. Mouhat and F. Coudert. Necessary and Sufficient Elastic Stability Conditions in Various Crystal Systems. Physical Review B, 90(22):224104, 2014. https://doi.org/10.1103/PhysRevB.90.224104.

[39] P. Hartley, R. G. Egdell, K. H. L. Zhang, M. V. Hohmann, L. F. J. Piper, D. J. Morgan, D. O. Scanlon, B. A. D. Williamson, and A. Regoutz. Experimental and Theoretical Study of the Electronic Structures of Lanthanide Indium Perovskites $LnInO_3$. The Journal of Physical Chemistry C, 125:6387–6400, 2021. https://dx.doi.org/10.1021/acs.jpcc.0c11592.

[40] C. S. Kamal, T. K. V. Rao, P. V. S. S. S. N. Reddy, K. Sujatha, B. P. Ajayi, J. B. Jasinski, and K. R. Rao. Unravelling the energy transfer mechanism in bismuth co-activation of $LaInO_3 : Sm^{3+}/Ho^{3+}$ nanophosphor for color-tunable luminescence. RSC Advances, 7(16):9724–9731, 2017. http://xlink.rsc.org/?DOI=c6ra28719k.

[41] F. Bloch. Über die Quantenmechanik der Elektronen in Kristallgittern. Zeitschrift für Physik, 52:555–600, 1929. http://dx.doi.org/10.1007/BF01339455.

[42] ScienceDirect. Spherical harmonic. https://www.sciencedirect.com/topics/mathematics/spherical-harmonic, accessed: February 23, 2026.

[43] The density-functional toolkit. Periodic problems and plane-wave discretisations. https://docs.dftk.org/stable/guide/periodic_problems, accessed: March 10, 2026.

[44] exciting Sodium. Input reference for exciting sodium. http://exciting.wikidot.com/ref:input, accessed: March 10, 2026.

[45] C. Carbogno. Theoretical material science: Electronic structure theory at the computer. https://www3.itp.tu-berlin.de/fileadmin/a3233/upload/SS17/TMS/SS17_TMS_Ex_5_CompScript.pdf, accessed: March 02, 2026.

[46] R. P. Feynman. Forces in Molecules. Physical Review, 56:340–343, 1939. https://doi.org/10.1103/PhysRev.56.340.

[47] R. H. Byrd, P. Lu, J. Nocedal, and C. Zhu. A Limited Memory Algorithm for Bound Constrained Optimization. SIAM Journal on Scientific Computing, 16 (5):1190–1208, 1995. https://doi.org/10.1137/0916069.

[48] J. M. Rondinelli, B. Deng, and L. D. Marks. Enhancing structure relaxations for first-principles codes: An approximate Hessian approach. Computational Materials Science, 40(3):345–353, 2007. https://doi.org/10.1016/j.commatsci.2007.01.004.

[49] W. Aggoune, C. Draxl, and D. Nabok. Nomad repository: In4la4o12 exciting simulation. https://nomad-lab.eu/prod/v1/gui/search/entries/entry/id/aPj4IEEGrDPghvqQd5DLV-twAGOh, accessed: January 23, 2026.

[50] G. Kresse and J. Furthmüller. Efficient iterative schemes for ab initio total-energy calculations using a plane-wave basis set. Physical Review B, 54(16): 11169–11186, 1996. https://doi.org/10.1103/PhysRevB.54.11169.

[51] S. J. Clark, M. D. Segall, C. J. Pickard, P. J. Hasnip, M. I. J. Probert, and K. Refson und M. C. Payne. First principles methods using CASTEP. Zeitschrift fuer Kristallographie. New crystal structures, 220(5-6):567–570, 2005. http://dx.doi.org/10.1524/zkri.220.5.567.65075.

[52] V. Blum, R. Gehrke, F. Hanke, P. Havu, V. Havu, X. Ren, K. Reuter, and M. Scheffler. Ab initio molecular simulations with numeric atom-centered orbitals. Computer Physics Communications, 180(11):2175–2196, 2009. https://doi.org/10.1016/j.cpc.2009.06.022.

[53] A. Erba R. Dovesi, R. Orlando, C. M. Zicovich-Wilson, B. Civalleri, S. Casassa, L. Maschio, M. Ferrabone, M. de la Pierre, P. D'Arco, Y. Noël, M. Causà, M. Rérat, and B. Kirtman. CRYSTAL14: A program for the ab initio investigation of crystalline solids. International Journal of Quantum Chemistry, 114 (19):1287–1317, 2014. https://doi.org/10.1002/qua.24658.

[54] P. Blaha, K. Schwarz, F. Tran, R. Laskowski, G. K. H. Madsen, and L. D. Marks. WIEN2k: An Augmented Plane Wave Plus Local Orbitals Program for Calculating Crystal Properties. The Journal of Chemical Physics, 152: 074101, 2020. https://doi.org/10.1063/1.5143061.

[55] X. Gonze, B. Amadon, P.-M. Anglade, J.-M. Beuken, F. Bottin, P. Boulanger, F. Bruneval, D. Caliste, R. Caracas, M. Côté, T. Deutsch, L. Genovese, Ph. Ghosez, M. Giantomassi, S. Goedecker, D.R. Hamann, P. Hermet, F. Jollet, G. Jomard, S. Leroux, M. Mancini, S. Mazevet, M.J.T. Oliveira, G. Onida, Y. Pouillon, T. Rangel, G.-M. Rignanese, D. Sangalli, R. Shaltaf, M. Torrent, M.J. Verstraete, G. Zerah, and J.W. Zwanziger. ABINIT: First-principles approach to material and nanosystem properties. Computer Physics Communications, 180(12):2582–2615, 2009. https://doi.org/10.1016/j.cpc.2009.07.007.

[56] P. Giannozzi, S. Baroni, N. Bonini, M. Calandra, R. Car, C. Cavazzoni, D. Ceresoli, G. L. Chiarotti, M. Cococcioni, I. Dabo, A. dal Corso, S. de Gironcoli, S. Fabris, G. Fratesi, R. Gebauer, U. Gerstmann, C. Gougoussis, A. Kokalj, M. Lazzeri, L. Martin-Samos, N. Marzari, F. Mauri, R. Mazzarello, S. Paolini, A. Pasquarello, L. Paulatto, C. Sbraccia, S. Scandolo, G. Sclauzero, A. P. Seitsonen, A. Smogunov, P. Umari, and R. M. Wentzcovitch. QUANTUM ESPRESSO: a modular and open-source software project for quantum simulations of materials. Journal of Physics: Condensed Matter, 21(39):395502, 2009. https://doi.org/10.1088/0953-8984/21/39/395502.

[57] A. S. Verma and A. Kumar. Bulk modulus of cubic perovskites. Journal of Alloys and Compounds, 541:210–214, 2012. https://doi.org/10.1016/j.jallcom.2012.07.027.

[58] E. Moreira, J. M. Henriques, D. L. Azevedo, E. W. S. Caetano, V. N. Freire, U. L. Fulco, and E. L. Albuquerque. Structural and optoelec-

tronic properties, and infrared spectrum of cubic $BaSnO_3$ from first principles calculations. Journal of Applied Physics, 112(4):043703, 2012. https://doi.org/10.1063/1.4745873.

[59] A. Bouhemadou and K. Haddadi. Structural, elastic, electronic and thermal properties of the cubic perovskite-type BaSnO3. Solid State Sciences, 12(4): 630–636, 2010. https://doi.org/10.1016/j.solidstatesciences.2010.01.020.

[60] M. Zupancic, W. Aggoune, T. Markurt, Y. Kim, Y M. Kim, K. Char, C. Draxl, and M. Albrecht. The role of the interface in controlling the epitaxial relationship between orthorhombic LaInO3 and cubic BaSnO3. Physical Review Materials, 4:123605, 2020. https://doi.org/10.1103/PhysRevMaterials.4.123605.

[61] Materials Project. $BaSnO_3$. `https://legacy.materialsproject.org/materials/mp-3163/`, accessed: March 15, 2026.

[62] Y. Wang, R. Sui, M. Bi, W. Tang, and S. Ma. Strain sensitivity of band structure and electron mobility in perovskite BaSnO 3 : First-principles calculation. RSC Advances, 9(25):14072–14077, 2019. https://doi.org/10.1039/C9RA02146A.

[63] D. O. Scanlon. Defect engineering of BaSnO3 for high-performance transparent conducting oxide applications. Physical Review B, 87(16):161201, 2013. https://doi.org/10.1103/PhysRevB.87.161201.

[64] E. H. Mountstevens, J. P. Attfield, and S. A. T. Redfern. Cation-size control of structural phase transitions in tin perovskites. Journal of Physics: Condensed Matter, 15(49):8315–8326, 2003. http://stacks.iop.org/0953-8984/15/8315/cm3_49_010.pdf.

[65] T. Maekawa, K. Kurosaki, and S. Yamanaka. Thermal and mechanical properties of polycrystalline BaSnO3. Journal of Alloys and Compounds, 416(1-2): 214–217, 2006. https://doi.org/10.1016/j.jallcom.2005.08.032.

[66] A. Prodjosantoso, Q. Zhou, and B. J. Kennedy. Synchrotron X-ray diffraction study of the Ba1SrSnO3 solid solution. Journal of Solid State Chemistry, 200: 241–245, 2013. https://doi.org/10.1016/j.jssc.2013.01.015.

[67] M. de Jong, W. Chen, T. Angsten, A. Jain, R. Notestine, A. Gamst, M. Sluiter, C. K. Ande, S. van der Zwaag, J. J. Plata, C. Toher, S. Curtarolo, G. Ceder, K. A. Persson, and M. Asta. Charting the complete elastic

properties of inorganic crystalline compounds. Scientific Data, 2(1):150009, 2015. https://doi.org/10.1038/sdata.2015.9.

[68] T. M. Duarte, P. G. C. Buzolin, I. M. G. Santos, E. Longo, and J. R. Sambrano. Choice of hybrid functional and basis set optimization to calculate the structural, electronic, mechanical, and vibrational properties of BaSnO3. Theoretical Chemistry Accounts, 135(6):151, 2016. https://dx.doi.org/10.1007/s00214-016-1901-1.

[69] A. Guendouz, K. D. Khodja, and B. Amrani. First-principle study origin of ferromagnetism in non-magnetic perovskite BaSnO3 doped with 2p-X (X=C, N). Revista Mexicana de Física, 70(6):061602, 2024. https://doi.org/10.31349/RevMexFis.70.061602.

[70] E. Bévillon, A. Chesnaud, Y. Wang, G. Dezanneau, and G. Geneste. Theoretical and experimental study of the structural, dynamical and dielectric properties of perovskite BaSnO3. Journal of Physics: Condensed Matter, 20 (14):145217, 2008. https://doi.org/10.1088/0953-8984/20/14/145217.

[71] G. Murtaza and I. Ahmad. First principle study of the structural and optoelectronic properties of cubic perovskites CsPbM3 (M=Cl, Br, I). Physica B: Condensed Matter, 406(17):3222–3229, 2011. https://doi.org/10.1016/j.physb.2011.05.028.

[72] Y. H. Chang and C. H. Park. First-Principles Study of the Structural and the Electronic Properties of the Lead-Halide-Based Inorganic-Organic Perovskites (CH3NH3)PbX3 and CsPbX3 (X = Cl, Br, I). Journal of the Korean Physical Society, 44(4):889–893, 2004. https://www.osti.gov/etdeweb/biblio/21346142.

[73] M. Afsari, A. Boochani, and M. Hantezadeh. Electronic, optical and elastic properties of cubic perovskite CsPbI3: Using first principles study. Optik, 127 (23):11433–11443, 2016. https://doi.org/10.1016/j.ijleo.2016.09.013.

[74] Materials Project. $CsPbI_3$. `https://legacy.materialsproject.org/materials/mp-1069538/`, accessed: March 15, 2026.

[75] M. Aktary, M. Kamruzzaman, and R. Afrose. A comparative study of the mechanical stability, electronic, optical and photocatalytic properties of CsPbX3 (X = Cl, Br, I) by DFT calculations for optoelectronic applications. RSC Advances, 12(36):23704–23717, 2022. https://doi.org/10.1039/D2RA04591E.

[76] S. M. J. Zaidi, M. S. U. Saharb, M. I. Khanc, H. T. Alid, M. Khalide, and M. Shahid. A comparative DFT assessment of the mechanical, elastic, electronic, and optical parametric study of perovskites CsPbX3 for opto-electronic applications. Digest Journal of Nanomaterials and Biostructures, 19(3):1227–1241, 2024. https://doi.org/10.15251/DJNB.2024.193.1227.

[77] A. B. Alruqi and N. O. Ongwen. First principles investigation of elastic, electronic and thermoelectric properties of lead-free Cs–X–I (X = Pb, Gd, Nd, Y) perovskites. Journal of Physics Communications, 8(12):125004, 2024. https://doi.org/10.1088/2399-6528/ad8da8.

[78] S. Idrissi, H. Labrim, L. Bahmad, and A. Benyoussef. DFT and TDDFT studies of the new inorganic perovskite CsPbI3 for solar cell applications. Chemical Physics Letters, 766:138347, 2021. https://doi.org/10.1016/j.cplett.2021.138347.

[79] H. M. Ghaithan, S. M. H. Qaid, Z. A. Alahmed, H. S. Bawazir, and A. S. Aldwayyan. Electronic Structure and Optical Properties of Inorganic Pm3m and Pnma CsPbX3 (X = Cl, Br, I) Perovskite: A Theoretical Understanding from Density Functional Theory Calculations. Materials, 16(18):6232, 2023. https://doi.org/10.3390/ma16186232.

[80] D. M. Trots and S. V. Myagkota. High-temperature structural evolution of caesium and rubidium triiodoplumbates. Journal of Physics and Chemistry of Solids, 69(10):2520– 2526, 2008. https://doi.org/10.1016/j.jpcs.2008.05.007.

[81] Y. Yuan, R. Xu, H. Xu, F. Hong, F. Xu, and L. Wang. Nature of the band gap of halide perovskites ABX 3 (A = CH 3 NH 3 , Cs; B = Sn, Pb; X = Cl, Br, I): First-principles calculations. Chinese Physics B, 24(11):116302, 2015. https://doi.org/10.1088/1674-1056/24/11/116302.

[82] A. Marronnier, G. Roma, S. Boyer-Richard, L. Pedesseau, J. Jancu, Y. Bonnassieux, C. Katan, C. C. Stoumpos, M. G. Kanatzidis, and J. Even. Anharmonicity and Disorder in the Black Phases of Cesium Lead Iodide Used for Stable Inorganic Perovskite Solar Cells. ACS Nano, 12(4):3477–3486, 2018. https://doi.org/10.1021/acsnano.8b00267.

[83] G. E. Eperon, G. M. Paternò, R. J. Sutton, A. Zampetti, A. A. Haghighirad, F. Caciallibc, and H. J. Snaith. Inorganic caesium lead iodide perovskite solar cells. Journal of Materials Chemistry A, 3(39):19688–19695, 2015. https://doi.org/10.1039/C5TA06398A.

[84] M. Roknuzzaman, K. Ostrikov, H. Wang, A. Du, and T. Tesfamichael. Towards lead-free perovskite photovoltaics and optoelectronics by ab-initio simulations. Scientific Reports, 7(1):14025, 2017. https://doi.org/10.1038/s41598-017-13172-y.

[85] M. A. Fadla, B. Bentria, T. Dahame, and A. Benghia. First-principles investigation on the stability and material properties of all-inorganic cesium lead iodide perovskites CsPbI3 polymorphs. Physica B: Condensed Matter, 585: 412118, 2020. https://doi.org/10.1016/j.physb.2020.412118.

[86] N. A. Koshi, K. Thekkepat, D. Lee, S. Lee, and S. Bhattacharjee. Multi-site mixing and entropy stabilization of CsPbI3 with potential application in photovoltaics. Materials Science, 2025. https://doi.org/10.48550/arXiv.2504.18272.

[87] H. Jin, J. Im, and A. J. Freeman. Topological insulator phase in halide perovskite structures. Physical Review B, 86:121102, 2012. https://doi.org/10.1103/PhysRevB.86.121102.

[88] Y. Rakita, S. R. Cohen, N. K. Kedem, G. Hodes, and D. Cahen. Mechanical properties of APbX3 (A = Cs or CH3NH3; X= I or Br) perovskite single crystals. MRS Communications, 5(4):623–629, 2015. https://doi.org/10.1557/mrc.2015.69.

[89] A. Erkişi, G. Gökoğlub, G. Sürücüc, R. Ellialtıoğlua, and E. K. Yıldırım. First-principles investigation of LaGaO3 and LaInO3 lanthanum perovskite oxides. Philosophical Magazine, 96(19):2040–2058, 2016. https://doi.org/10.1080/14786435.2016.1189100.

[90] Materials Project. $LaInO_3$. `https://legacy.materialsproject.org/materials/mp-11623/`, accessed: March 15, 2026.

[91] R. Ubic and G. Subodh. The prediction of lattice constants in orthorhombic perovskites. Journal of Alloys and Compounds, 488(1):374–379, 2009. https://doi.org/10.1016/j.jallcom.2009.08.139.

[92] D. H. Jang, W. Lee, E. Sohn, H. J. Kim, D. Seo, J. Park, E. J. Choi, and K. H. Kim. Single crystal growth and optical properties of a transparent perovskite oxide LaInO3. Journal of Applied Physics, 121(12):125109, 2017. http://dx.doi.org/10.1063/1.4977863.

[93] H. M. Park, H. J. Lee, S. H. Park, and H. I. Yoo. Lanthanum indium oxide from X-ray powder diffraction. Acta

Crystallographica Section C: Structural Chemistry, 59(12):i131–i132, 2003. https://doi.org/10.1107/S0108270103024806.

[94] F. Mouhat and F. Coudert. Necessary and Sufficient Elastic Stability Conditions in Various Crystal Systems. Physical Review B, 90(22), 2014. https://doi.org/10.1103/PhysRevB.90.224104.

[95] N. Pandech, K. Sarasamak, and S. Limpijumnong. Elastic properties of perovskite ATiO3 (A = Be, Mg, Ca, Sr, and Ba) and PbBO3 (B = Ti, Zr, and Hf): First principles calculations. Journal of Applied Physics, 117(17):174108, 2015. https://doi.org/10.1063/1.4919837.

[96] A. C. Ferreira, A. Létoublon, S. Paofai, S. Raymond, C. Ecolivet, B. Rufflé, S. Cordier, C. Katan, M. I. Saidaminov, A. A. Zhumekenov, O. M. Bakr, J. Even, and P. Bourges. Elastic Softness of Hybrid Lead Halide Perovskites. Physical Review Letters, 121(8):085502, 2018. https://doi.org/10.1103/PhysRevLett.121.085502.

[97] G. Zhang, A. M. Reilly, A. Tkatchenko1, and M. Scheffler. Performance of various density-functional approximations for cohesive properties of 64 bulk solids. New Journal of Physics, 20(6):063020, 2018. https://doi.org/10.1088/1367-2630/aac7f0.

[98] M. Råsander and M. A. Moram. On the accuracy of commonly used density functional approximations in determining the elastic constants of insulators and semiconductors. Journal of Chemical Physics, 143(14):144104, 2015. https://doi.org/10.1063/1.4932334.

[99] S. Bächli. Implementing Third-Order Elastic Coefficients in ElaStic. Humboldt Universität zu Berlin, 2024.

[100] A. Pandit and A. Bongiorno. A first-principles method to calculate fourth-order elastic constants of solid materials. Computer Physics Communications, 288:108751, 2023. https://doi.org/10.1016/j.cpc.2023.108751.

[101] S. Shikata, T. Tanno, T. Teraji, H. Kanda, T. Yamada, and J. Kushibiki. Precise measurements of diamond lattice constant using Bond method. Japanese Journal of Applied Physics, 57(11):111301, 2018. https://doi.org/10.7567/jjap.57.111301.

[102] O. Madelung, U. Rössler, and M. Schulz. Springer Materials. Springer-Verlag GmbH, 1998.

[103] M. Barhoumi, D. Rocca, M. Said, and S. Lebègue. Elastic and mechanical properties of cubic diamond and silicon using density functional theory and the random phase approximation. Solid State Communications, 324:114136, 2021. https://doi.org/10.1016/j.ssc.2020.114136.

[104] A. V. Telichko, S. V. Erohin, G. M. Kvashnin, P. B. Sorokin, B. P. Sorokin, and V. D. Blank. Diamond's third-order elastic constants: ab initio calculations and experimental investigation. Journal of Materials Science, 52:3447–3456, 2017. https://doi.org/10.1007/s10853-016-0633-x.

[105] A. Migliori, H. Ledbetter, R. G. Leisure, C. Pantea, and J. B. Betts. Diamond's elastic stiffnesses from 322 K to 10 K. Journal of Applied Physics, 104(5): 053512, 2008. https://doi.org/10.1063/1.2975190.

[106] K. J. Gray. Electromagnetic window properties of CVD diamond. Proceedings of SPIE - The International Society for Optical Engineering, 1759:203–208, 1992. https://doi.org/10.1117/12.130773.

Appendix A

Species files

The species files specify which (l, m) channels are included in the basis expansion of the LAPW basis set for every type of atom, see Listing A.1. Afterwards, the local orbitals used are included, Listing A.2 shows an extract of this part. Both examples are from the species file for the Pb-atom (lead), which appears in the cubic perovskite $CsPbI_3$. All other 7 species files will be uploaded along with the respective calculations on the NOMAD repository [10].

Listing A.1: Atomic orbitals included in the species file Pb.xml.

```
<sp chemicalSymbol="Pb" name="lead" z="-82.0000" mass="377702.4941">
  <muffinTin rmin="0.100000E-06" radius="2.0000" rinf="27.5273"
     radialmeshPoints="800"/>
  <atomicState n="1" l="0" kappa="1" occ="2.00000" core="true"/>
  <atomicState n="2" l="0" kappa="1" occ="2.00000" core="true"/>
  <atomicState n="2" l="1" kappa="1" occ="2.00000" core="true"/>
  <atomicState n="2" l="1" kappa="2" occ="4.00000" core="true"/>
  <atomicState n="3" l="0" kappa="1" occ="2.00000" core="true"/>
  <atomicState n="3" l="1" kappa="1" occ="2.00000" core="true"/>
  <atomicState n="3" l="1" kappa="2" occ="4.00000" core="true"/>
  <atomicState n="3" l="2" kappa="2" occ="4.00000" core="true"/>
  <atomicState n="3" l="2" kappa="3" occ="6.00000" core="true"/>
  <atomicState n="4" l="0" kappa="1" occ="2.00000" core="true"/>
  <atomicState n="4" l="1" kappa="1" occ="2.00000" core="true"/>
  <atomicState n="4" l="1" kappa="2" occ="4.00000" core="true"/>
  <atomicState n="4" l="2" kappa="2" occ="4.00000" core="true"/>
  <atomicState n="4" l="2" kappa="3" occ="6.00000" core="true"/>
  <atomicState n="4" l="3" kappa="3" occ="6.00000" core="false"/>
  <atomicState n="4" l="3" kappa="4" occ="8.00000" core="false"/>
  <atomicState n="5" l="0" kappa="1" occ="2.00000" core="false"/>
  <atomicState n="5" l="1" kappa="1" occ="2.00000" core="false"/>
  <atomicState n="5" l="1" kappa="2" occ="4.00000" core="false"/>
  <atomicState n="5" l="2" kappa="2" occ="4.00000" core="false"/>
  <atomicState n="5" l="2" kappa="3" occ="6.00000" core="false"/>
  <atomicState n="6" l="0" kappa="1" occ="2.00000" core="false"/>
  <atomicState n="6" l="1" kappa="1" occ="1.00000" core="false"/>
  <atomicState n="6" l="1" kappa="2" occ="1.00000" core="false"/>
```

Listing A.2: Extract of the local orbitals included in the species file Pb.xml.

```
<default type="lapw" trialEnergy="0.1500" searchE="false"/>

     <custom l="0" type="lapw" trialEnergy="-0.150" searchE="false"/>
     <lo l="0">
       <wf matchingOrder="0" trialEnergy="-0.150" searchE="false"/>
       <wf matchingOrder="1" trialEnergy="-0.150" searchE="false"/>
     </lo>
     <lo l="0">
       <wf matchingOrder="0" trialEnergy="-0.150" searchE="false"/>
       <wf matchingOrder="0" trialEnergy="-4.900" searchE="false"/>
     </lo>
     <lo l="0">
       <wf matchingOrder="0" trialEnergy="-4.900" searchE="false"/>
       <wf matchingOrder="1" trialEnergy="-4.900" searchE="false"/>
     </lo>
     <lo l="0">
       <wf matchingOrder="0" trialEnergy="-4.900" searchE="false"/>
       <wf matchingOrder="2" trialEnergy="-4.900" searchE="false"/>
     </lo>
     <custom l="1" type="lapw" trialEnergy="0.1500" searchE="false"/>
     <lo l="1">
       <wf matchingOrder="0" trialEnergy="0.1500" searchE="false"/>
       <wf matchingOrder="1" trialEnergy="0.1500" searchE="false"/>
     </lo>
     <lo l="1">
       <wf matchingOrder="0" trialEnergy="0.1500" searchE="false"/>
       <wf matchingOrder="2" trialEnergy="0.1500" searchE="false"/>
     </lo>
     <lo l="1">
       <wf matchingOrder="0" trialEnergy="0.1500" searchE="false"/>
       <wf matchingOrder="0" trialEnergy="-2.720" searchE="false"/>
     </lo>

     <lo l="1">
       <wf matchingOrder="0" trialEnergy="-2.720" searchE="false"/>
       <wf matchingOrder="1" trialEnergy="-2.720" searchE="false"/>
     </lo>
```

Appendix B

Input files

An example for the structure of an input file for **exciting** is shown here in Listing B.1. The investigated crystal in this case is $BaSnO_3$. The crystal scale at the top gives the form of the unit cell. In this case, the cell is not distorted and belongs to the equilibrium structure of $BaSnO_3$ for the PBEsol functional. In the computational cell this material has one Ba atom, one Sb atom, and three O atoms. The respective muffin tin radii R_α from Section 3.1 are specified next to the atom types. In the ⟨**groundstate**⟩ element, the important attributes **rgkmax**, **ngridk**, and **gmaxvr** from Section 3.1 are given. The exchange-correlation functional is specified here too with the attribute **xctype**. After this, if the ⟨**relax**⟩ element is given, then an internal structural relaxation will be performed after the self-consistent convergence of the electron density.

Listing B.1: Input file for **exciting** for the cubic perovskite $BaSnO_3$.

```
<input>

  <title> BaSnO3 </title>

  <structure speciespath="/users/sol/herrmanh/SPECIES">

  <crystal scale="7.8018">
    <basevect>1.0 0.0 0.0</basevect>
    <basevect>0.0 1.0 0.0</basevect>
    <basevect>0.0 0.0 1.0</basevect>
  </crystal>

  <species speciesfile="Ba.xml" rmt="2.2">
    <atom coord="0.0 0.0 0.0"/>
  </species>

  <species speciesfile="Sn.xml" rmt="2.0">
    <atom coord="0.5 0.5 0.5"/>
  </species>

  <species speciesfile="O.xml" rmt="1.6">
    <atom coord="0.5 0.5 0.0"/>
    <atom coord="0.0 0.5 0.5"/>
    <atom coord="0.5 0.0 0.5"/>
  </species>
  </structure>

<groundstate
   ngridk="14 14 14"
   gmaxvr="25"
   swidth="0.0001"
   rgkmax="9"
   xctype="GGA_PBE_SOL">
</groundstate>

<relax/>

</input>
```

Appendix C

Convergence studies

Convergence studies were done for the bulk modulus B, observing the deviations in this value for slightly changed input parameters. See Table C.1 for $BaSnO_3$, Table C.2 for $CsPbI_3$, and Table C.3 for $LaInO_3$. The bulk modulus is a combination of elastic constants that can be obtained by only one series of isotropic volume distortions, which makes it suitable for convergence studies. Each **bold** entry for every functional in the tables refers to the parameters that were used for the calculation of the elastic properties which we discussed in Section 4.4. The bulk moduli there exhibit a systematic deviation from the values used for convergence here, simply because `ElaStic` makes use of a polynomial to fit the data in the energy curve, while here the Birch-Murnaghan equation of state was used in the fits. The input parameters are given in the columns of the tables. The `nempty` value gives the number of empty states or unoccupied states that are included in the expansion [44]. This parameter is important for the hybrid functionals.

For pair-wise comparisons of the parameters a convergence within 1% of the bulk modulus is achieved in most cases, in some within 2% of the bulk modulus. However, there is a notable residual dependence on `nempty` in the two hybrids PBE0 and HSE for the material $CsPbI_3$. The choice of 100 is only converged in a range of about 3% of the bulk modulus. The convergence calculation with a value of `nempty` = 140 shows that convergence here is significantly slower than for the local and semilocal exchange-correlation functionals. A strict convergence would have required significantly higher values of `nempty`. `exciting` calculations with a high value of this parameter are very demanding though and we had to opt for a compromise, settling with a convergence of the bulk modulus within approximately 3%. Despite this relatively high error, the overall trends between different functionals remain unaffected. The results are considered sufficiently accurate for the purpose of this work.

Table C.1: Convergence calculations for the bulk modulus B of $BaSnO_3$. All results are given in GPa. r: `rgkmax`, k: `ngridk`, g: `gmaxvr`, n: `nempty`. In the cubic symmetry, all three values of k are the same, so only one is shown here. If n is not specified, then the default value of `nempty` was used, which is 5. The **bold** entries are the used sets of parameters.

Functional	r	k	g	n	B
LDA	**9**	**14**	**18**		161.69
	9	16	18		161.70
	9.5	14	18		161.65
	9.5	16	20		161.66
PBE	**9**	**14**	**25**		130.81
	9	16	25		130.83
	8.5	14	25		130.12
	9.5	16	27		131.17
PBEsol	**9**	**14**	**25**		147.79
	9	16	25		147.80
	9.5	14	25		147.75
	9.5	16	27		148.09
PBE0	**8**	**6**	**25**	**40**	163.77
	8	8	25	40	164.16
	8.5	6	25	40	163.70
	8	6	25		166.83
	8.5	8	27		167.00
	7	8	25	40	164.92
	7	8	25	100	165.09
HSE	**8**	**6**	**25**	**40**	162.31
	8	6	25	100	162.38
	8	8	25	40	162.68
	8.5	6	25	40	162.32
	8	6	25		165.12
	8.5	8	27		165.18

Table C.2: Convergence calculations for the bulk modulus B of $CsPbI_3$. All results are given in GPa. r: `rgkmax`, k: `ngridk`, g: `gmaxvr`, n: `nempty`. In the cubic symmetry, all three values of k are the same, so only one is shown here. If n is not specified, then the default value of `nempty` was used, which is 5. The **bold** entries are the used sets of parameters.

Functional	r	k	g	n	B
LDA	**9**	**14**	**18**		19.58
	9	16	18		19.59
	9.5	14	18		19.56
	9.5	16	20		19.56
PBE	**9**	**14**	**25**		13.92
	9	16	25		13.92
	9.5	14	25		13.92
	9.5	16	27		13.92
PBEsol	**9**	**14**	**25**		16.49
	9	16	25		16.49
	9.5	14	25		16.46
	9.5	16	27		16.47
PBE0	**8**	**6**	**25**	**100**	17.48
	8	8	25	100	17.26
	8	4	25	100	17.89
	8	6	25	40	16.51
	8	8	25	40	16.41
	8.5	6	25	40	16.36
	8	6	25	140	18.03
HSE	**8**	**6**	**25**	**100**	17.42
	8	6	25	40	16.44
	8	8	25	40	16.31
	8.5	6	25	40	16.17
	8	6	25	140	17.97

Table C.3: Convergence calculations for the bulk modulus B of $LaInO_3$. All results are given in GPa. r: `rgkmax`, k: `ngridk`, g: `gmaxvr`. The default value `nempty` $= 5$ was used. The **bold** entries are the used sets of parameters.

Functional	r	k	g	B
LDA	**8**	**4×3×4**	**18**	165.19
	8	6×4×6	18	165.27
	8.5	4×3×4	18	165.23
	8.5	6×4×6	20	165.16
	7	3×2×3	20	163.89
PBE	**8**	**4×3×4**	**25**	137.22
	8	6×4×6	25	137.22
	8.5	4×3×4	25	137.22
	8.5	6×4×6	27	137.22
	7	3×2×3	27	138.29
PBEsol	**8**	**4×3×4**	**25**	151.92
	8	6×4×6	25	151.85
	8.5	4×3×4	25	151.85
	8.5	6×4×6	27	151.85
	7	3×2×3	27	152.49

Appendix D

Diamond reference calculations

Reference calculations with bulk diamond were done, since it is an inexpensive material in **exciting** calculations, having only two C-atoms in its unit cell. Lattice constants can be found in Table D.1, elastic constants in Table D.2, and elastic moduli in Table D.3—along with theoretical and experimental reference values. The table structure is the same as in Chapter 4. The following input parameters were used: **rgkmax** = 9, **ngridk** = 14×14×14, **gmaxvr** = 25 (20 for LDA).

Table D.1: Lattice parameters for diamond. All results are given in Angstrom.

Reference	Code/Exp.	Type	a
This work	**exciting**	LDA	3.534
		PBE	3.572
		PBEsol	3.555
		PBE0	3.545
		HSE	3.544
Råsander and Moram [98]	VASP	LDA	3.533
		PBE	3.570
		PBEsol	3.553
		PBE0	3.543
		HSE	3.543
Pandit and Bongiorno [100]	QE	PBE	3.57
Shikata *et al.* [101]	Exp.		3.5671
Madelung *et al.* [102]	Exp.		3.545

Table D.2: Elastic constants for diamond. All results are given in GPa.

Reference	Code/Exp.	Type	C_{11}	C_{12}	C_{44}
This work	**exciting**	LDA	1103.2	147.9	592.0
		PBE	1052.6	124.5	558.7
		PBEsol	1069.4	139.2	572.6
		PBE0	1134.5	139.2	610.1
		HSE	1135.4	139.9	610.4
Råsander and Moram [98]	VASP	LDA	1106	149	594
		PBE	1056	125	560
		PBEsol	1075	141	577
		PBE0	1145	138	613
		HSE	1143	138	611
Barhoumi *et al.* [103]	VASP	LDA	1105.6	149.4	592.6
		PBE	1053	125	560.2
		HSE	1141.6	140.2	620
Pandit and Bongiorno [100]	QE	PBE	1054	124	559
Telichko *et al.* [104]	Exp.		1082	125	579
Madelung *et al.* [102]	Exp.		1079	124	578
Migliori *et al.* [105]	Exp.		1079.26	126.73	578.16

Table D.3: Elastic moduli for diamond: Bulk modulus B, shear modulus G, and Young modulus Y. All results are given in GPa. An (*) indicates that the moduli were not mentioned explicitly in the respective reference, but computed here using the elastic constants from the reference.

Reference	Code/Exp.	Type	B	G	Y
This work	**exciting**	LDA	466.3	546.3	1178.6
		PBE	433.9	520.8	1116.0
		PBEsol	449.3	529.6	1140.6
		PBE0	471.0	565.1	1211.0
		HSE	471.7	565.3	1211.9
Råsander and Moram [98]	VASP	LDA	468	547*	1181*
		PBE	436	522*	1119*
		PBEsol	452	533*	1148*
		PBE0	473	569*	1218*
		HSE	473	568*	1217*
Barhoumi *et al.* [103]	VASP	LDA	468.13	543.63	1176
		PBE	434.30	519.5	1114.3
		HSE	474	569	1219.4
Madelung *et al.* [102]	Exp.		462		
Gray [106]	Exp.		442	514	1180

Acknowledgments

I thank Pasquale for his supervision. I thank Sven for letting me use his species files. I thank Marti, Kshitij, and Joris for their help. And last but not least, I thank Emily for her emotional support.

Selbstständigkeitserklärung

Ich erkläre hiermit, dass ich die vorliegende Arbeit selbstständig verfasst und noch nicht für andere Prüfungen eingereicht habe. Sämtliche Quellen einschließlich Internetquellen, die unverändert oder abgewandelt wiedergegeben werden, insbesondere Quellen für Texte, Grafiken, Tabellen, Bilder sowie die Nutzung von Künstlicher Intelligenz für die Erstellung von Texten und Abbildungen, sind als solche kenntlich gemacht. Mir ist bekannt, dass bei Verstößen gegen diese Grundsätze ein Verfahren wegen Täuschungsversuchs bzw. Täuschung eingeleitet wird.

Berlin, 06.04.2026

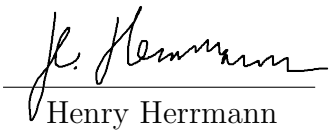

Henry Herrmann